CM² MAGAZINE

第 39 期

南方科技大学海洋磁学中心主编

创刊词

海洋是生命的摇篮，是文明的纽带。地球上最早的生命诞生于海洋，海洋里的生命最终进化成了人类，人类的文化融合又通过海洋得以实现。人因海而兴。

人类对海洋的探索从未停止。从远古时代美丽的神话传说，到麦哲伦的全球航行，再到现代对大洋的科学钻探计划，海洋逐渐从人类敬畏崇拜幻想的精神寄托演变成可以开发利用与科学研究的客观存在。其中，上个世纪与太空探索同步发展的大洋科学钻探计划将人类对海洋的认知推向了崭新的纬度：深海（deep sea）与深时（deep time）。大洋钻探计划让人类知道，奔流不息的大海之下，埋藏的却是亿万年的地球历史。它们记录了地球板块的运动，从而使板块构造学说得到证实；它们记录了地球环境的演变，从而让古海洋学方兴未艾。

在探索海洋的悠久历史中，从大航海时代的导航，到大洋钻探计划中不可或缺的磁性地层学，磁学发挥了不可替代的作用。这不是偶然，因为从微观到宏观，磁性是最基本的物理属性之一，可以说，万物皆有磁性。基于课题组的学科背景和对海洋的理解，我们对海洋的探索以磁学为主要手段，海洋磁学中心因此而生。

海洋磁学中心，简称 CM^2，一为其全名“Centre for Marine Magnetism”的缩写，另者恰与爱因斯坦著名的质能方程 $E = MC^2$ 对称，借以表达我们对科学巨匠的敬仰和对科学的不懈追求。

然而科学从来不是单打独斗的产物。我们以磁学为研究海洋的主攻利器，但绝不仅限于磁学。凡与磁学相关的领域均是我们关注的重点。为了跟踪反映国内外地球科学特别是与磁学有关的地球科学领域的最新研究进展，海洋磁学中心特地主办 CM^2 Magazine，以期与各位地球科学工作者相互交流学习、合作共进！

“海洋孕育了生命，联通了世界，促进了发展”。 21 世纪是海洋科学的时代，由陆向海，让我们携手迈进中国海洋科学的黄金时代。

目 录

海磁快讯

科普时报：科普是打通学科壁垒的桥梁

刘青松

自然界中很多生物非常聪明。章鱼可以轻松地逃离迷宫；乌鸦知道用树枝勾虫子；宠物犬可以和主人进行沟通；大猩猩更是可以学会手语……这些智慧，一部分写在基因里，成为本能；另外一部分需要通过传承和学习传给下一代。虽然在知识传承和学习效率方面，动物的学习系统无法与人类媲美。

其实，早期人类的知识传承效率其实也不高，在百万年尺度上，石器制作技能并没有特别大的变化。没有技术革新，就没有新的生活方式和组织模式。人类社会发展在原始模式下虽然步履坚定，但是进展缓慢，仿佛时间凝固一般。当人类创造了文字和书写工具后，知识积累变得容易，在这个基础上，知识积累和技术革新增速就水到渠成，人类文明的快车无法再停下来。

在人类文明发展中，谁占据了知识和创新的制高点，谁就能最大化地调动社会资源与能源，从而占领生存制高点。在工业革命之后，这种模式就变成了社会发展的主流，知识就是力量，高科技就是民族生存的未来。因此，如何快速地知识积累与传承，就成为人类面临的首要课题。

可是，现今社会人类传统学习模式与知识大爆炸并不匹配。对于大部分科研工作者，从幼儿园 3-4 岁开始接受基本教育到 30 岁左右博士后出站，要接受差不多近 30 年的时间积累，才开始基本懂得如何独立做科研。我们无法想象，100 年后，如果还是靠目前的学习方式，如何能传承人类庞大的知识体系。所以，提升知识传承效率，建立正确的知识传承体系就显得尤为必要。

传统高等教育有两个特色：阶梯方式和分科方式。对于阶梯方式，知识从浅入深，逐层传授。我们需要一种模式，打穿这种层级壁垒。显然，科普就是一种非常高效的手段。通过科普，把高层级知识合理引入到低层级，形成瀑布效应。为了适应时代发展，科学逐步变成分科之学。学科之间存在着壁垒。打通这

种壁垒，学科交叉才是科学最原始的本质。显然，科普就是不同学科之间的“普通话”，是学科壁垒之间的桥梁。她为大众认识现代高科技铺平道路。

现今是一个高科技飞跃的时代，形成了科学、技术与工程最前沿的新技术群。作为新兴的研究和生产体系，她代表着一个国家在国际上的竞争力，深刻地影响到人类文明发展，对一个民族的未来至关重要。

第 29 章　胶黄铁矿（Fe3S4）

铁硫化物是一个特殊的体系。其中包括强磁性的胶黄铁矿（Fe_3S_4）和磁黄铁矿（Fe_7S_8）。如果在充分还原的环境里，最稳定的硫化产物是黄铁矿（FeS_2）。

和磁铁矿一类比，我们就会发现胶黄铁矿和磁铁矿一样具有反尖晶石结构。由于 S 的离子半径比 O 的离子半径要大，所以单位体积内的铁离子含量会小，因此它的 Ms 也要随之减小。

M_S = 23-30 $Am^2/kg \approx$ ¼ 磁铁矿 M_S

B_C = 20-30 mT　　（比磁铁矿要高一些）

由于胶黄铁矿具有热不稳定性，测量胶黄铁矿的居里温度一直是个难题。研究表明，其居里温度（Chang et al.，2008）

T_C ~ 320-400℃

与磁铁矿不一样，胶黄铁矿的易磁化轴一直在<100>方向（Heywood et al.，1990），所以它不具备磁铁矿那样的低温转换特征，但是在经过 LTC 处理后，一样会退磁。

研究胶黄铁矿比较多的学者主要包括 Mark Dekkers、Andrew Roberts, 常燎等几位教授。Roberts 教授的贡献是发现胶黄铁矿远比过去认为的分布要广泛。常燎教授则系统研究了实验室合成的纯胶黄铁矿样品，对不同粒径胶黄铁矿的性质进行了详细的厘定。

胶黄铁矿是一种中间产物，其形成的机制有两种：

第一种是向黄铁矿转化的过程被打断，从而停留在中间状态。在台湾地区大量存在胶黄铁矿。我们可以这样解释，台湾这几个百万年以来一直处于快速隆升，在构造过程中，容易形成这种“打断”机制，使得胶黄铁矿保留下来。

第二种是硫的含量相对较少，不足以形成黄铁矿。以前的模型一直认为胶黄铁矿要在氧化还原界面之下形成。最近刘建兴博士的研究发现一个重要线索。他系统研究了黄海和渤海的沉积物，发现胶黄铁矿的出现常常伴有 Cd 含量增加。

我们知道 Cd 容易与微量 S 形成 CdS，在氧化还原界面沉淀下来。Cd 的峰值一般认为是弱氧化-弱还原环境，也就是氧化还原界面。这种一致性说明胶黄铁矿应该在氧化还原界面处形成。黄海和渤海属于边缘海，水深很浅。所以随着海进与海退，氧化还原界面会发生重要变化，所以胶黄铁矿会生成。只要胶黄铁矿一出现，就暗示着有水环境。所以胶黄铁矿可以被用来研究这些地区的海进情况以及海平面升降等过程。

Rowan 博士是 Roberts 教授的博士生。在读博士期间，他研究了沉积物中胶黄铁矿的生成过程。在沉积物浅部属于氧化环境，原生磁铁矿会得以保存。随着深度增加，逐渐转向还原环境，原生磁铁矿就会发生部分溶解。最开始小颗粒磁铁矿优先溶解，所以磁铁矿的整体粒径分布向粗颗粒方向移动，但是整体磁性会降低。深度再增加，原生磁铁矿会被大幅度溶解，胶黄铁矿会逐渐生成。自然界中形成的胶黄铁矿一般处于 SD 状态，成葡萄状集合在一起，磁相互作用很强，其 FORC 是典型的牛眼状特征，非常易于识别。其剩磁会在 300 多度快速下降，这也是确认胶黄铁矿主要证据之一。

上述过程在 Day 图上表现为一个逆时针旋转过程。粒径先粗后细，最后逐渐向 SD 颗粒方向转化。

如果样品含有胶黄铁矿，在 AF 退磁过程中，非常容易获得旋转剩磁（GRM）。具体表现为在 50-60 mT 之上，剩磁不但不下降，反而会逐渐升高。这对于传统的交变退磁绝对是一个干扰。很多情况下，只能用 60 mT 之下的退磁数据来确定古地磁场的方向。

段宗奇博士对这个现象进行了系统研究（Duan et al., 2020, G^3）。他在研究中国南海样品时就发现了这个现象。他对 GRM 很强的样品测量了 FORC 图，发现了两个独立的牛眼圈，一个矫顽力小，对应着 SD 磁铁矿。另外一个的矫顽力偏高，对应着胶黄铁矿。对样品进行 300 ℃加热处理，胶黄铁矿受热不稳定分解。之后再做 FORC 图，就会发现胶黄铁矿的牛眼圈消失了，同时热处理后的样品也不获得 GRM 了。这充分说明胶黄铁矿对 GRM 的贡献。同时，也有效地证明了前期加热 300 °，是消除胶黄铁矿 GRM 干扰的有效方法。

胶黄铁矿不只产生 GRM，它还能对整个磁性地层产生干扰。刘建兴博士在研究黄海样品时，在 MBB 边界附近发现多次“极性倒转行为”。如果按照传统

的思路，会直接把这些“极性倒转”与 GPTS 一一对应，从而建立年龄框架。可是，随后的研究发现，有的极性倒转层对应着胶黄铁矿富集层。这说明某些极性倒转其实不是真实的信息，而是由于胶黄铁矿造成的。只有把这些干扰信息去除掉，才能得到准确的年龄框架，并和生物地层年代框架完美统一。

那么胶黄铁矿是如何记录这种反向磁化的呢？

胶黄铁矿自己不具有反向磁化的能力。于是葛坤朋博士利用微磁模拟技术对 MD 磁铁矿和 SD 胶黄铁矿体系进行了研究。他发现 MD 颗粒聚集在一起的时候，会形成涡旋磁化。有的方位磁场是正向磁化，有的则是反向磁化。在这些反向磁化 MD 磁铁矿旁边，如果生成 SD 胶黄铁矿，受 MD 颗粒涡旋磁矩的影响，这些 SD 胶黄铁矿就会记录反向磁化。随着还原程度加强，MD 颗粒的磁铁矿会被溶解，最终就只剩下这些反向磁化的胶黄铁矿。

文献速递

1. 过去 25 万年来地中海外流受控于从热带到冰盖区的淡水输入

翻译人：仲义 zhongy@sustech.edu.cn

Francisco J. Sierro, David A. Hodell, Nils Andersen., et al., Mediterranean Overflow over the last 250 kyr: Freshwater forcing from the tropics to the Ice Sheets [J] Paleoceanography and Paleoclimatology, 2020, 35(9), e2020PA003931.

https://doi.org/10.1029/2020PA003931

摘要：为了探索过去进入大西洋的地中海外流（MOW）的变化，我们基于直布罗陀海峡附近的卡迪斯湾的 IODP U1389 站位，讨论过去 25 万年以来 MOW 强度变化及底栖有孔虫的 $\delta^{13}C$ 的变化特征。结果显示 MOW 强度变化和底栖有孔虫的 $\delta^{13}C$ 主要受控于岁差控制下的地中海水文通量变化。岁差高值时由于尼罗河释放减弱和地中海年降水降低导致了直布罗陀海峡的 MOW 强度增强和地中海环流增大，反之亦然。在千年尺度上，由于格林兰岛在冰阶之间更多热量和淡水释放到大气中，增加了东地中海的热量损失。这将导致大西洋水的密度梯度增强，导致卡迪斯湾内 MOW 流速增强。与非海因里希（Heinrich）事件不同，在 Heinrich 事件期间表现出的流速小范围增强，而在中间阶段流速明显减弱。这种减弱的 MOW 在 Heinrich 1 和 11 期最为明显。而这些更低流速是由于劳伦和欧亚冰盖的淡水释放引起的大西洋中层水密度降低导致的 MOW 下沉导致。Heinrich 事件时期大西洋较深处的盐度和热量的侵入和该事件结束时期的减少是导致大西洋经向环流在气候终止期发生变化的重要原因之一。

ABSTRACT: To investigate past changes in the Mediterranean Overflow Water (MOW) to the Atlantic, we analyzed the strength of the MOW and benthic δ13C along the last 250 kyr at Integrated Ocean Drilling Program (IODP) Site U1389 in the Gulf of Cadiz, near the Strait of Gibraltar. Both the strength of the MOW and the benthic δ13C were mainly driven by precession-controlled fluctuations in the Mediterranean hydrologic budget. Reduced/enhanced

Nile discharge and lower/higher Mediterranean annual rainfall at precession maxima/minima resulted in higher/lower MOW strengths at Gibraltar and stronger/weaker Mediterranean overturning circulation. At millennial scale, the higher heat and freshwater loss to the atmosphere during Greenland stadials increased buoyancy loss in the eastern Mediterranean. This enhanced the density gradient with Atlantic water, resulting in a higher MOW velocity in the Gulf of Cadiz. Unlike non‐Heinrich stadials, a lower‐amplitude increase in velocity was seen during Heinrich stadials (HSs), and a significant drop in velocity was recorded in the middle phase. This weak MOW was especially recognized in Termination I and II during HS1 and HS11. These lower velocities at the depth of Site U1389 were triggered by MOW deepening due to the lower densities of Atlantic intermediate water caused by freshwater released from the Laurentide and Eurasian ice sheets. The intrusion of salt and heat at deeper depths in the Atlantic during HSs and its shoaling at the end could have contributed to drive the changes in the Atlantic Meridional Overturning Circulation during Terminations.

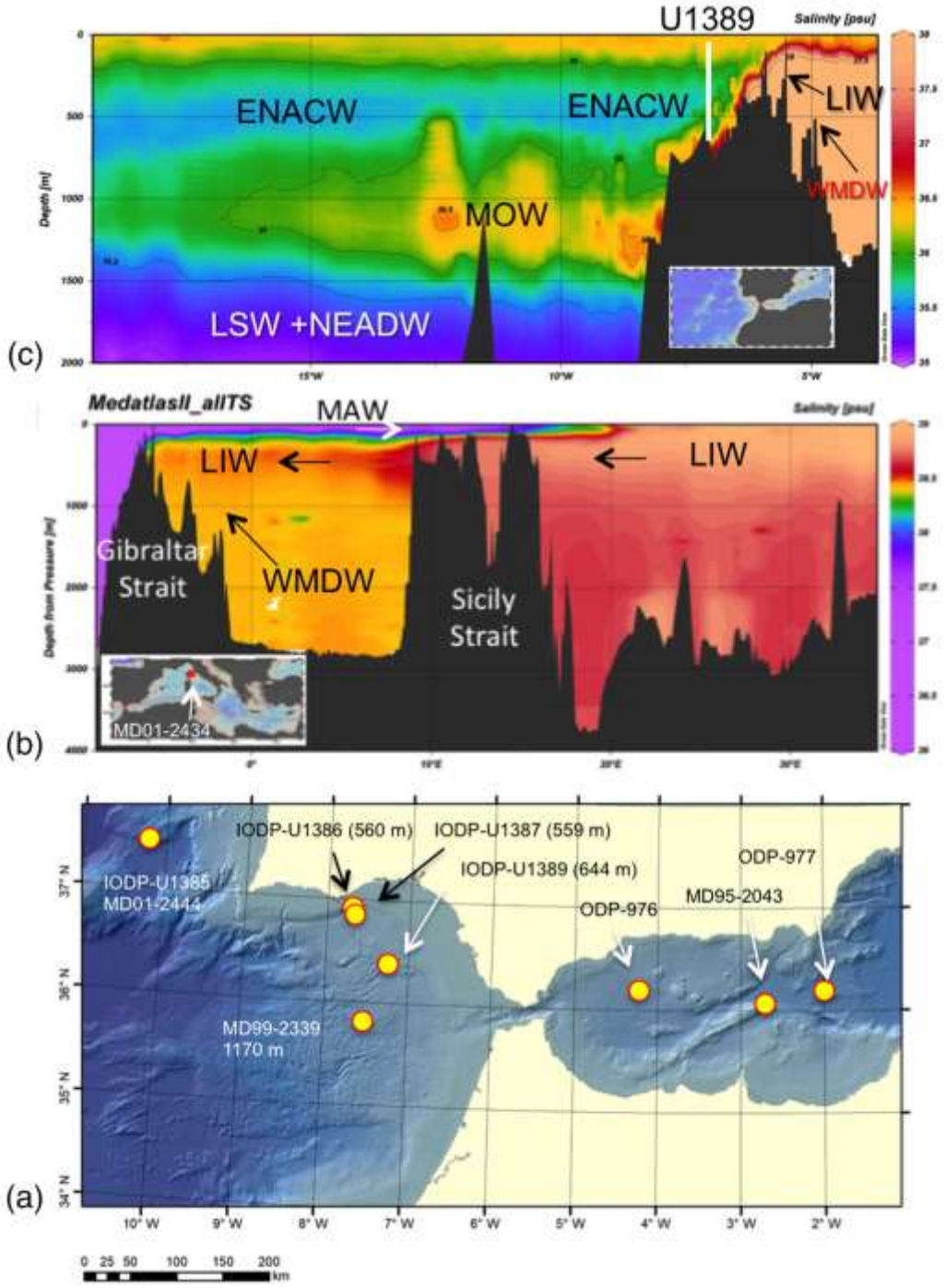

Figure 1. Location of the main cores mentioned in this study and hydrographic profiles of the NE Atlantic andMediterranean. (a) Salinity profile of the northeastern Atlantic, the Strait of Gibraltar, and the westernmost Mediterranean, showing the main water masses in the Alboran Sea, the descending branch of the MOW, and the tongue of MOW in the Atlantic (World Ocean Database, WOD2018, Boyer et al., 2018). (b) Salinity profile showing the zonal Mediterranean overturning circulation formed by the eastward Atlantic inflow formed by the modified Atlantic water (MAW) and the

westward Levantine intermediate water (LIW) (data from MedAtlas 2002 - Database (Fichaut et al., 2003). (c) Map location of IODP Site U1389 in the Gulf of Cadiz as well as other sites referred to in this study. Legend for water masses (in alphabetic order): ENACW ¼ east North Atlantic central water; LIW ¼ Levantine intermediate water; LSW ¼ Labrador Sea Water, MAW ¼ modified Atlantic water, MOW ¼ Mediterranean Overflow Water; NEADW ¼ northeast Atlantic deep water, and WMDW ¼ western Mediterranean deep water. The software Ocean Data View (Schlitzer, R., Ocean Data View, odv.awi.de, 2018) was used to generate the Atlantic and Mediterranean profiles.

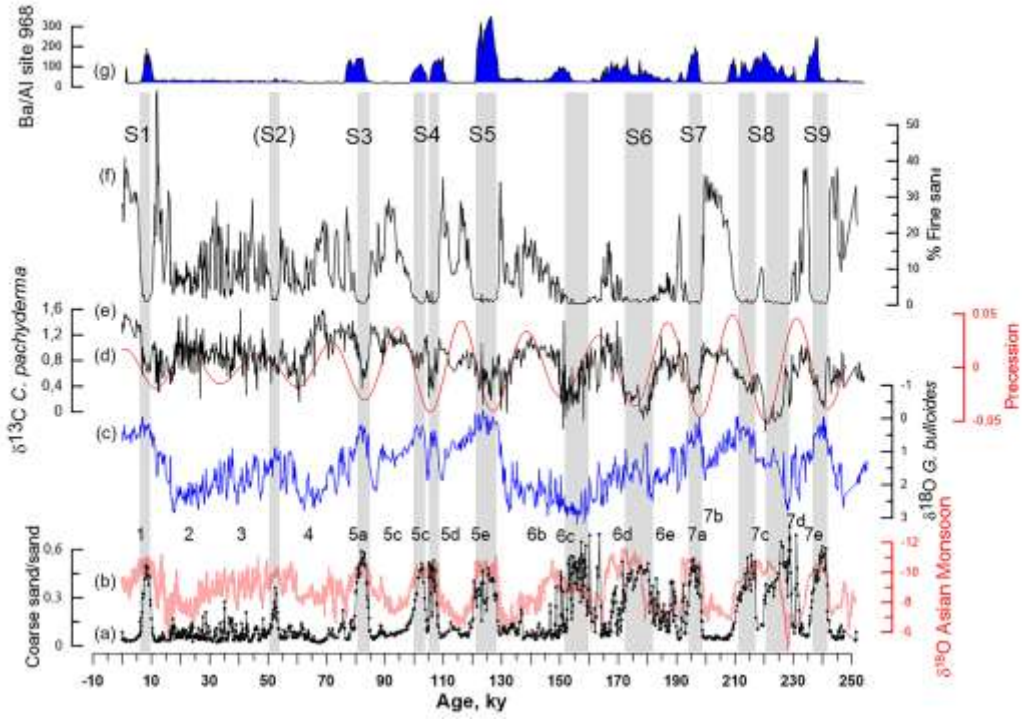

Figure 2. Correlation between events of reduced MOW strength at Site U1389, eastern Mediterranean stagnation events (sapropels), weak Mediterranean thermohaline circulation, and episodes of Asian Monsoon intensification. (a) Ratio of coarse sand/total sand (fraction >150 μm)/total sand. (b) δ18O from Asian speleothems (Cheng et al., 2016). (c) G.bulloides δ18O at Site U1389. (d) Precession index. (e) Cibicidoides pachyderma δ13C at Site U1389. (f) Percent fine sand
(fraction 62–150 μm) at Site U1389. (g) Ba/Al ratio at ODP Site 968 in the eastern Mediterranean (Ziegler et al., 2008). Gray bands indicate periods of weak MOW at the Strait of Gibraltar (lowest fine sand percentages). S1 to S9 denote Sapropels. MIS stages and substages after Railsback et al. (2015) are shown below the G. bulloides δ18O record.

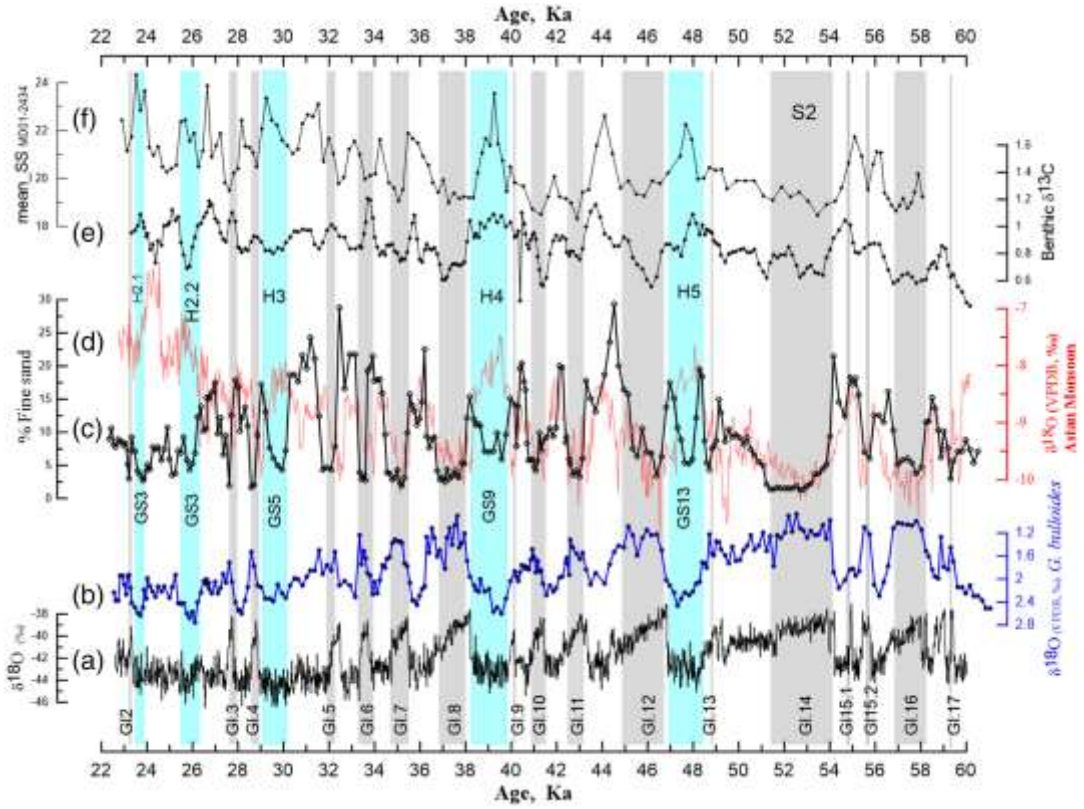

Figure 3. Millennial‐scale changes in MOW strength and Mediterranean overturning at Site U1389 during MIS 3. (a) δ18O NGRIP2 (‰ V‐SMOW) (North Greenland Ice Core Project members, 2004) with the GICC05 timescale(Rasmussen et al., 2014). (b) Globigerina bulloides δ18O from IODP Site U1389. (c) Percentage of fine sand (fraction 62–150 μm). (d) δ18O from Asian speleothems (Cheng et al., 2016) (red). (e) Cibicidoides pachyderma δ13C at Site U1389 (3 moving average). (f) Mean SS in the Corsica margin (MD01‐2434, Toucanne et al., 2012). Gray bands show Greenland interstadials. Blue bands show HSs. GI2 to GI17 denote Greenland interstadials. GS3 to GS13 denote Greenland stadials. S2 denotes Sapropel .

2. 地幔的碳是使地壳成矿物质富集的物理载体

翻译人：冯婉仪 fengwy@sustech.edu.cn

Knott T R, Branney M J, Reichow M K, et al. ***Fluxing of mantle carbon as a physical agent for metallogenic fertilization of the crust****[J]. Nature communication, 2020, 11: 4342.*

https://doi.org/10.1038/s41467-020-18157-6

摘要：岩浆系统对于在地壳中挥发分和主要存在于地幔中的元素（包括经济上重要的金属，如：镍、铜和铂族元素）的富集起着至关重要的作用。然而，这些金属元素在硅酸盐岩浆中的迁移主要发生在稠密的硫化物液体中，这些液体易于合并和沉淀，因此，金属元素不能在上升的岩浆中被有效地迁移。在这里，我们展示了岩石矿物结构的观察结果以及碳和氧同位素数据，这些观察结果和同位素数据表明，在一些位于大陆地壳底部的镁铁质-超镁铁质岩浆系统中，幔源碳酸盐和硫化物之间存在着密切的联系。我们认为碳作为一种具有浮力的超临界 CO_2 流体，可能是一种神秘的、能促进硫化物在地幔-地壳转换带迁移的物理载体。这可能是一种常见但神秘的机制，它能促使挥发分和金属元素从地幔循环至中-下大陆地壳中，但当岩浆到达地球表面时，它却几乎没有留下什么痕迹。

ABSTRACT: Magmatic systems play a crucial role in enriching the crust with volatiles and elements that reside primarily within the Earth's mantle, including economically important metals like nickel, copper and platinum-group elements. However, transport of these metals within silicate magmas primarily occurs within dense sulfide liquids, which tend to coalesce, settle and not be efficiently transported in ascending magmas. Here we show textural observations, backed up with carbon and oxygen isotope data, which indicate an intimate association between mantle-derived carbonates and sulfides in some mafic-ultramafic magmatic systems emplaced at the base of the continental crust. We propose that carbon, as a buoyant supercritical CO_2 fluid, might be a covert agent aiding and promoting the physical transport of sulfides across the mantle-crust transition. This may be a common but cryptic mechanism that facilitates cycling of volatiles and metals from the mantle to the lower-to-mid continental crust, which leaves little footprint behind by the time magmas reach the Earth's surface.

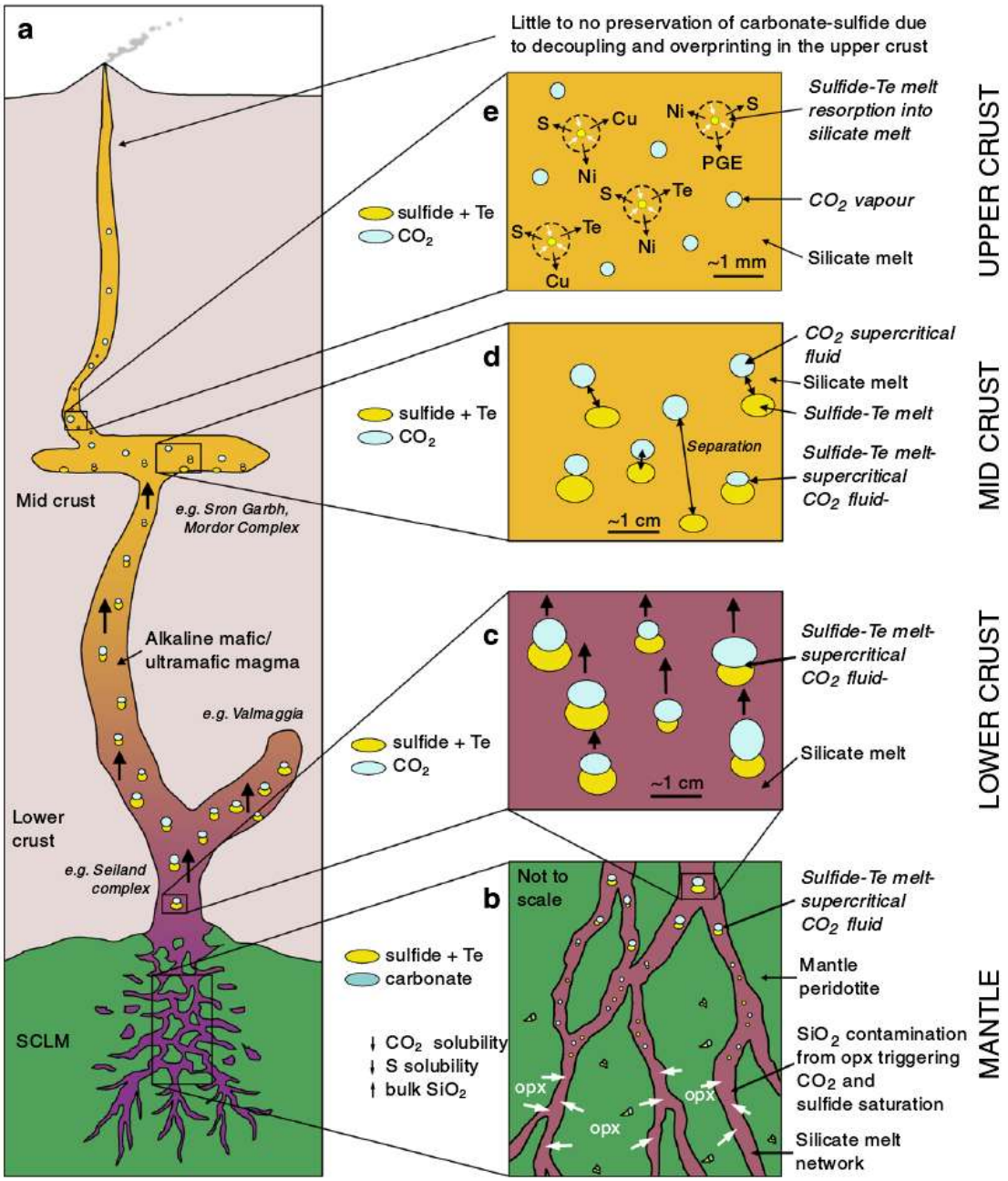

Figure 1. Model showing the role of C in transporting metal-rich sulfides from the mantle into the crust. a Schematic representation of mantle to crust magmatic systems as represented by our case studies. Not to scale; b migration of low-degree partial melts reacting with orthopyroxene (opx) causing SiO_2 contamination triggering CO_2 and sulfide supersaturation; c upward migration of metal-rich sulfide melts by physical attraction to droplets of low density supercritical CO_2-rich fluid; d mid-crustal separation of supercritical CO_2-rich fluid and sulfide melts; e mid- to upper crustal redissolution of sulfide into silicate melt and further decoupling from CO_2.

3. 早白垩纪 Rajmahal 玄武岩的古地磁和岩石磁学结果：对印度次大陆古地理学和 Kerguelen 热点迁移的意义

翻译人:李园洁 liyj3@sustech.edu.cn

Kapawar M.R., Venkateshwarlu Mamilla. ***Paleomagnetism and rock magnetism of early Cretaceous Rajmahal basalts, NE India: Implications for paleogeography of the Indian subcontinent and migration of the Kerguelen hotspot. Journal of Asian Earth Sciences****, 2020, 201. https://doi.org/10.1016/j.jseaes.2020.104517*

摘要：本文从印度 Rajmahal Traps (RT)18 个点（90 个样品）的 350 个标准样本获得新的古地磁和岩石磁学的结果。详细的岩石磁学结果表明单畴的磁铁矿是主要的载磁矿物，并伴有钛铁矿，黄铁矿和磁赤铁矿。计算出特征剩磁方向，平均磁偏角 317.51°和平均磁倾角−61.92° (α_{95} = 3.6°; k = 93.39)，获得 RT 在~117 Ma 虚地磁极（VGP）的位置在 11.37° N, 297.58° E (62.42° W) ，A95 = 3.5°, k = 99.99, dp = 4.33, dm = 5.58，计算出的古纬度 43.1° S 与前人研究一致。RT 玄武岩的古地磁极具有很小的长期变化，与轴向偶极子场模型一致。印度的视极移曲线上的 VGP 与前人的结果吻合很好。本文的结果与地幔柱迁移和全球地幔循环的假说一致，表明 Kerguelen 热点（地幔柱）向南迁移最少 6°。

ABSTRACT：We present here new paleomagnetic and rock magnetic results from Rajmahal Traps (RT), India. The results are comprising of 350 standard specimens collected from 18 sites (90 samples). The detailed rock magnetic studies indicate that a Single Domain (SD) magnetite [Fe3O4] is the dominant magnetic carrier with ilmenite, pyrrhotite, and maghemite in the accessory form. The calculated Characteristic Remanent Magnetization (ChRM) directions yield a mean declination of 317.51°; mean inclination of −61.92° (α_{95} = 3.6°; k = 93.39). The obtained Virtual Geomagnetic Pole (VGP) position of the RT at ~117 Ma is 11.37°N, 297.58°E (62.42°W) with A95 = 3.5°; k = 99.99, dp = 4.33, dm = 5.58, and the calculated paleolatitude is at 43.1°S indistinguishable from that of earlier works. This paleomagnetic pole of RT basalts has minimal

effect of secular variation and comply with the Geocentric Axial Dipole (GAD) model. The VGP is plotted on synthetic Apparent Polar Wander Path (APWP) for India, constrained better, and agrees well with the previously reported poles. The postulation of migration of mantle plume and the global mantle circulations are tested, and the present study results are in accord with this, suggesting the southward migration of the Kerguelen hotspot (mantle plume) by at least 6 °.

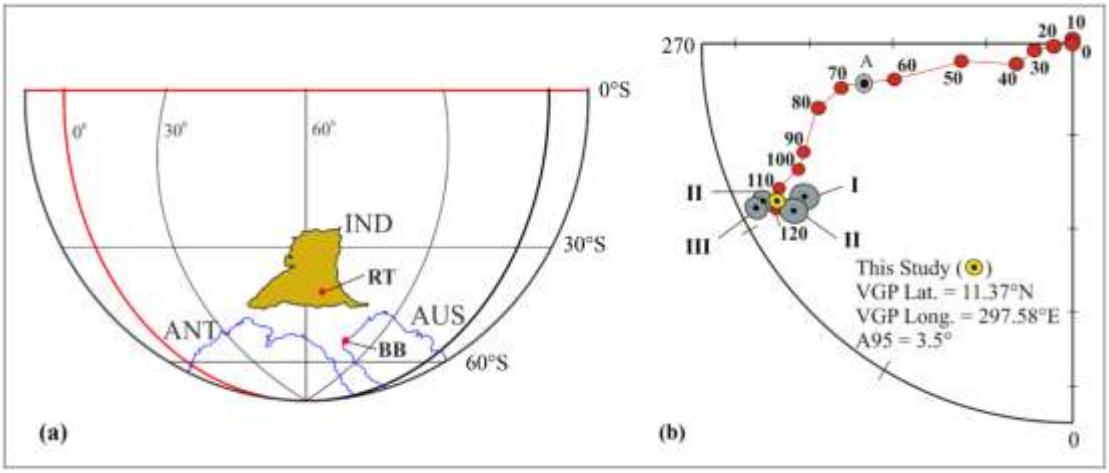

Figure 1. (a) The paleogeographic position of the Indian subcontinent at ~ 117 Ma (Early Cretaceous) determined from the present study. The RT denotes Rajmahal Traps near the eastern margin of the Indian subcontinent, BB corresponds to the Bunbury basalts at the western margin of Australia, and a paleolatitude of 52 ± 4° S is after Olierook et al. (2016). The Australian and Antarctica plates are put closer within permissible limits of geologic and paleomagnetic results (IND = India, AUS = Australia, and ANT = Antarctica). (b) The mean paleomagnetic pole data of the Rajmahal Traps plotted along the synthetic APWP for India based on the GAPWaP model by Torsvik et al. (2012). The black dot depicted with the value of A95 in a yellow circle between 110 and 120 Ma interval is the obtained VGP from this study [11.37° N, 297.58° E (62.42° W); A95 = 3.5° , k = 99.99]. We have depicted the other study results from RT and ST (of the RBS volcanic province) for comparison. The 'I' is a VGP from ST (16° N, 60° W; A95 = 7° ; Athavale et al., 1963), 'II' is a VGP from ST (12° N, 59° W; A95 = 7° ; Rao et al., 1993), 'III' is a VGP from RT (7° N, 63° W; A95 = 4° ; Klootwijk, 1971), and 'IV' is a VGP from RT (3° N, 62° W; A95 = 4° ; McDougall and McElhinny, 1970). The gray-colored circles indicate A95, around mean pole position. 'A' corresponds to the Deccan Super Pole (DSP, 36.9° N; 78.7° W) derived by Vandamme et al. (1991). (For interpretation of the references to colour in this figure legend, the reader is referred to the web version of this article).

4. 全球七个实验室的 XRF 岩芯扫描结果的比对和实用校准方法

翻译人：柳加波

Dunlea, A.G., Murray, R.W., Tada, R., Zarikian, C.A.A., 2020. Intercomparison of XRF Core Scanning Results From Seven Labs and Approaches to Practical Calibration Geochemistry , Geophysics , Geosystems. doi:10.1029/2020GC009248

摘要：海洋沉积物的 X 射线荧光（XRF）扫描能够获得接近连续且高分辨率的元素丰度记录，这些记录通常被解释为不同时间尺度上古海洋学过程的代用指标。但是，很多其他变量也会影响 XRF 扫描测量，从而影响元素丰度的定量校准和不同实验室的数据比较。通过对比不同实验室之间的 XRF 扫描结果和校准，是解决歧义和理解扫描结果的最佳方法。在这项研究中，我们发送了一组七个海洋沉积物断面（每个 1.5 m）供世界各地的七个 XRF 实验室进行扫描，通过比较不同实验室扫描结果，从而了解各种影响因素。实验室之间的每秒原始元素计数（cps）的结果不同，但是元素比率具有更高的可对比性。四个实验室还扫描了一组均质的沉积物颗粒，其成分由电感耦合等离子体发射光谱（ICP-OES）和 ICP-质谱（MS）确定，以两种方式将原始 XRF 元素的 cps 转换为浓度：线性校准和对数比校准。尽管两个校准曲线都拟合得很好，但结果表明，实验室之间的对数比校准数据比线性校准数据更具可对比性。小尺度（高分辨率）功能通常在不同扫描之间无法重现，因此应谨慎解释。除了实用校准的指导外，我们的研究还提出了最佳方法，以提高 XRF 扫描可获得的数据质量，从而有利于古海洋学研究。

ABSTRACT: X-ray fluorescence (XRF) scanning of marine sediment has the potential to yield near‐continuous and high‐resolution records of elemental abundances, which are often interpreted as proxies for paleoceanographic processes over different time scales. However, many other variables also affect scanning XRF measurements and convolute the quantitative calibrations of element abundances and comparisons of data from different labs. Extensive interlab comparisons of XRF scanning results and calibrations are essential to resolve ambiguities and to understand the best way to interpret the data produced. For this study, we sent a set of seven

marine sediment sections (1.5 m each) to be scanned by seven XRF facilities around the world to compare the outcomes amidst a myriad of factors influencing the results. Results of raw element counts per second (cps) were different between labs, but element ratios were more comparable. Four of the labs also scanned a set of homogenized sediment pellets with compositions determined by inductively coupled plasma‐optical emission spectrometry (ICP‐OES) and ICP‐mass spectrometry (MS) to convert the raw XRF element cps to concentrations in two ways: a linear calibration and a log‐ratio calibration. Although both calibration curves are well fit, the results show that the log‐ratio calibrated data are significantly more comparable between labs than the linearly calibrated data. Smaller-scale (higher‐resolution) features are often not reproducible between the different scans and should be interpreted with caution. Along with guidance on practical calibrations, our study recommends best practices to increase the quality of information that can be derived from scanning XRF to benefit the field of paleoceanography.

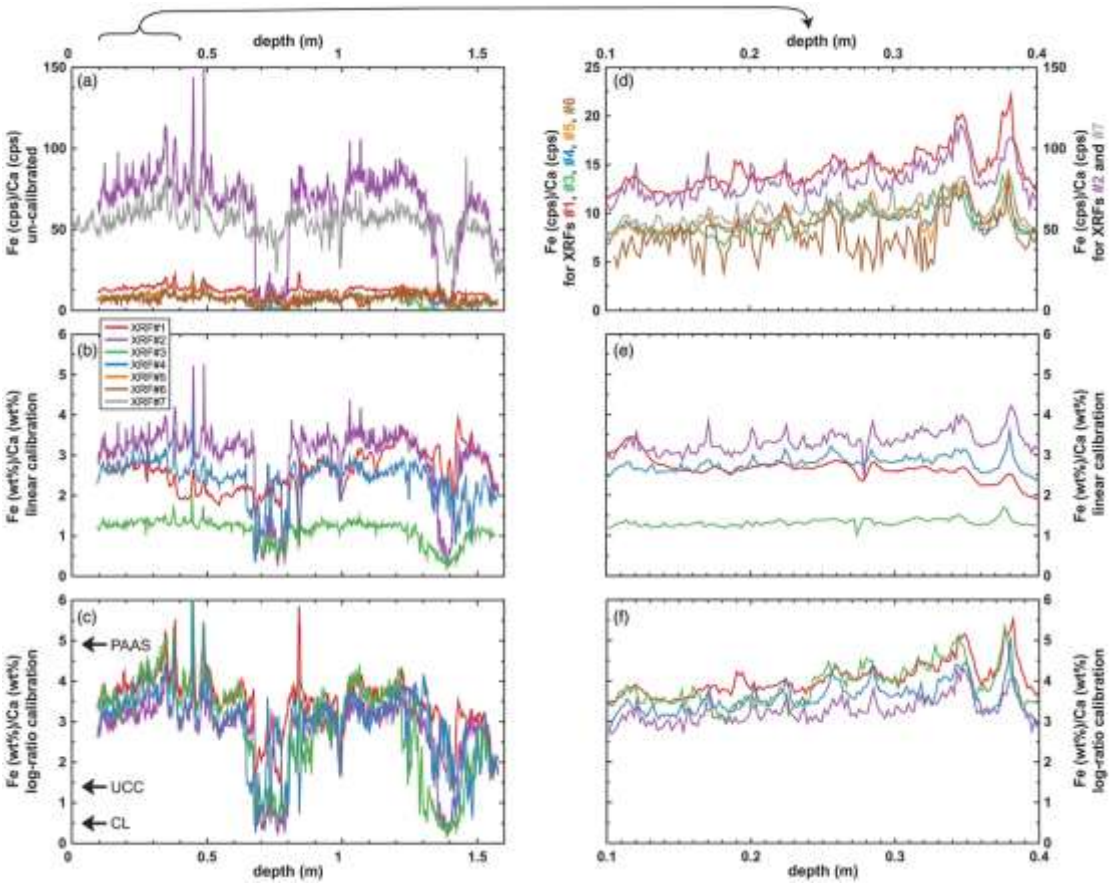

Figure 1: Comparison of ratios generated by scanning XRF for (a) raw, uncalibrated Fe (cps)/Ca (cps), (b) linearly calibrated Fe (wt%)/Ca (wt%), and (c) log‐ratio calibrated Fe (wt%)/Ca (wt%) with the Fe/Ca of Post‐Archean average Australian Shale (PAAS), upper continental crust (UCC), and Chinese Loess (CL) marked for reference. Only four labs scanned the pellet data and could be calibrated for (b) and (c). The *x* axis for each plot is depth in meters from the top of Section U1425C‐2H3. XRF#7 scanned the stratigraphically aligned sediment in Hole U1425D. Each color represents a different lab that scanned the sections (see legend). The scanning XRF records from the various labs are most comparable when they have been calibrated with log‐ratios. Plots (d)–(f) are the same as plots (a)–(c), respectively, but are zoomed up on 0.1–0.4 m below the top of the section to emphasize smaller scale comparability. Note the double *y* axes in (d).

5. 从古南海俯冲到南海残留洋脊俯冲---来自于北吕宋弧西部的同位素证据

翻译人：刘伟 inewway@163.com

Liu, H.-Q., Yumul Jr, G. P., Dimalanta, C. B., et al, ***Western Northern Luzon Isotopic Evidence of Transition From Proto‐South China Sea to South China Sea Fossil Ridge Subduction*** *[J]. Tectonics, 2020, 39(2).*

https://doi.org/10.1029/2019TC005639

摘要: 对北吕宋弧西部有代表性的岩浆岩进行了地球化学和年代学分析，以重建新生代构造。北吕宋弧西部的渐新世-更新世岩浆，其元素和 Sr‐Nd‐Hf‐Pb‐O 同位素地球化学特征与洋内弧（intraoceanic arc）岩浆活动相似，指示了来自地幔楔，并有分馏结晶。其中，渐新世-中新世(~26.8- 15.6 Ma) 的 CDDC（岩体的简称）样品 Sr-Nd 同位素呈负相关，指示了远洋沉积物释放的流体/熔体与地幔的交代作用。中新世-更新世样品(<~9 Ma)表现出稳定的 87Sr/86Sr 值和变化的 ε Nd 值，并与黄岩岛海山玄武岩有部分重叠，指示了黄岩岛海山玄武岩释放的流体/熔体与地幔的交代作用，响应于南海残留脊俯冲到北吕宋弧。台湾-吕宋弧岩浆作用也观察到了 Sr‐Nd‐Hf‐Pb 同位素的时间序列变化。渐新世-中新世(>~9 Ma)岩浆活动表现为洋内弧（intraoceanic arc）同位素特征，暗示了俯冲远洋沉积物的化学印迹。中新世-更新世(<~9 Ma)火山岩表现出富集的地幔型同位素组成，与地幔陆源沉积物输入相一致。台湾-吕宋岩浆活动的 Sr‐Nd‐Hf‐Pb 同位素特征，结合古地磁证据，反映了北吕宋弧西部记录了约 9 Ma 时由古南海俯冲向南海残留脊俯冲的过渡。此外，本研究还强调了弧陆碰撞体系中下覆板块相对富集组分在的年轻仰冲洋壳成熟过程中的重要性。

ABSTRACT: Temporal geochemical comparisons are conducted for representative magmatism from western Northern Luzon to reconstruct the Cenozoic tectonics. Oligo‐Pleistocene magmas from western Northern Luzon display elemental and Sr‐Nd‐Hf‐Pb‐O isotope geochemistry similar to intraoceanic arc magmatism, consistent with derivation from the mantle wedge, coupled with fractional crystallization. Specifically, the Oligo‐Miocene (~26.8–15.6 Ma) Central Cordillera diorite complex samples exhibit a negative correlation between Sr‐Nd isotopes, consistent with mantle metasomatism

by fluids/melts released from pelagic sediments. The Mio - Pleistocene samples (<~9 Ma) exhibit consistent 87Sr/86Sr ratios with variable ε Nd and partially overlap with those of Scarborough seamount basalts, consistent with mantle metasomatism by fluids/melts released from the Scarborough seamount basalts, which are being subducted beneath Northern Luzon with the South China Sea fossil ridge. Temporal changes in Sr - Nd - Hf - Pb isotopes are also observed for the Taiwan - Luzon arc magmatism. The Oligo - Miocene (>~9 Ma) magmatism exhibit intraoceanic arc isotopic signatures, suggestive of a chemical imprint from subducted pelagic sediments. The Mio - Pleistocene (<~9 Ma) lavas display enriched mantle - type isotope compositions, consistent with an input of terrigenous sediment in the mantle. The temporal variations in Sr - Nd - Hf - Pb isotopes for the Taiwan - Luzon magmatism, combined with paleomagnetic evidence, mirror a transition from the Proto - South China Sea to the South China Sea fossil ridge subduction beneath western Northern Luzon at ~9 Ma. In addition, this study also highlights the importance of relatively enriched components in the lower plate in the maturation of overriding juvenile oceanic crust in an arc - continent collision system.

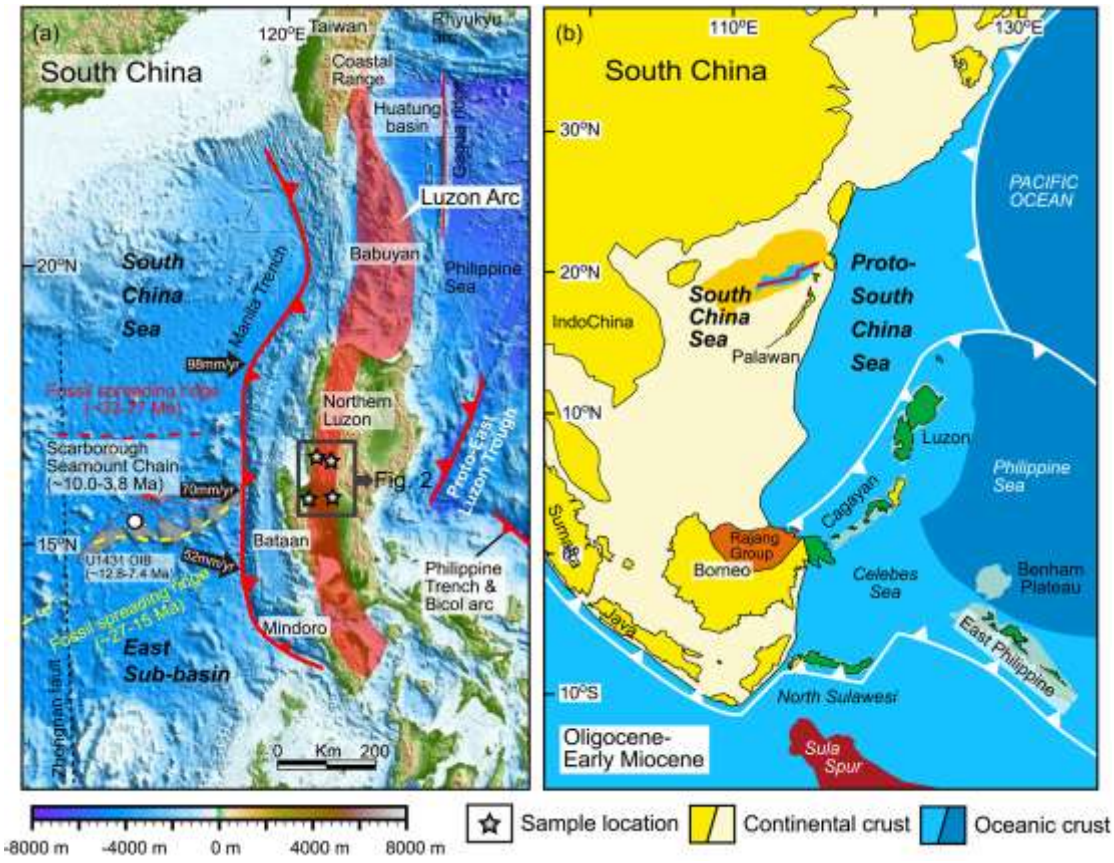

Figure 1. Tectonic framework showing main blocks and magmatism around the Luzon arc - Taiwan collision system (a) and paleogeographic reconstruction of southeastern Asia during Oligocene - early

Miocene (b, modified from Hall, 2012). Yellow and red dashed lines (a) denote the locations of final fossil ridges (~27–15 Ma) and ridge jump (~33–27 Ma), respectively (Li et al., 2014).

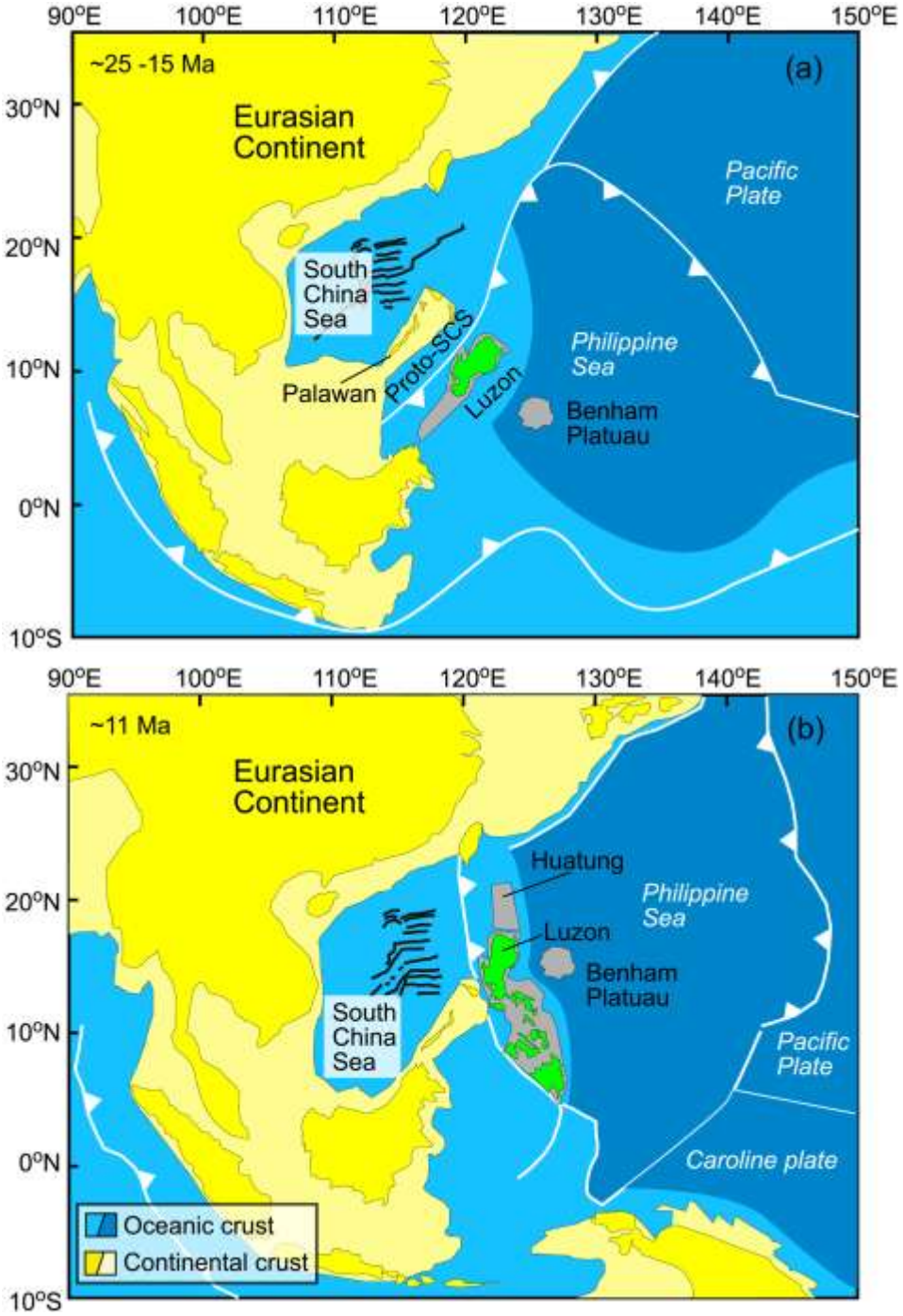

Figure 2. Schematic geologic map (modified from Queaño et al., 2007 and Hall, 2012) showing a tectonic transition from the Proto‐South China Sea subduction (a) to the South China Sea subduction (b) beneath western Northern Luzon at ~11 Ma. The Proto‐SCS denotes Proto‐South China Sea.

6. 通过卷积神经网络预测磁化方向

翻译人：曹伟 11930854@QQ.com

Felicia Nurindrawati & Jiajia Sun. ***Predicting Magnetization Directions Using Convolutional Neural Networks.*** *[J].* ***Journal of Geophysical Research (Solid Earth)****, 2020: 106551*

https://doi.org/10.1029/2020JB019675

摘要：磁测资料被广泛应用于了解盆地构造、矿床系统、各种地质系统的形成历史以及许多其他方面。磁测资料的正确解释需要对研究区域内磁源体的总磁化方向有准确的认识。现有的估计磁化方向的方法例如三维反演，要么存在不稳定的数据处理步骤，要么是计算密集型的过程。在本研究中，我们开发了一种利用卷积神经网络(CNN)自动预测磁源体磁化方向的新方法。CNN 方法在计算机视觉和地震图像解释等领域取得了巨大的成功，但还没有应用于磁性数据的参数提取。我们从一个合成源体中模拟了许多不同磁化方向的磁性参数图，所有这些磁性参数图都受同一背景场的影响。两个 CNN 系统各自进行训练，一个用于预测倾角，另一个用于预测偏角。通过系统地比较 13 种不同的 CNN 架构，我们确定了用于预测倾角和偏角的最优 CNN 架构。此外，我们还研究了磁化强度、源体形状和位置以及深度等参数对预测模型性能的影响。我们还利用澳大利亚黑山苏长岩和中国叶山地区的现场数据对该方法进行了测试，这些数据可用于比较之前的研究结果。我们的研究表明，机器学习提供了一种基于磁测图自动预测磁化方向的有效方法。

ABSTRACT: Magnetic data have been widely used for understanding basin structures, mineral deposit systems, formation history of various geological systems, and many others. Proper interpretation of magnetic data requires an accurate knowledge of total magnetization directions of the source bodies in an area of study. Existing approaches for estimating magnetization directions involve either unstable data processing steps or computationally intensive processes such as 3D inversions. In this study, we developed a new method of automatically predicting the magnetization direction of a magnetic source body using Convolutional Neural Networks (CNN). CNNs have achieved great success in many other applications such as computer vision and seismic image interpretation, but have not been used to extract parameters from magnetic data. We

simulated many magnetic data maps with different magnetization directions from a synthetic source body, all subject to the same background field. Two CNNs were trained separately, one for predicting the inclination and the other for predicting declination. We determined the optimal CNN architectures for predicting inclinations and declinations by systematically comparing 13 different CNN architectures. In addition, we investigated the effect of having different parameters such as magnetization magnitude, source body shape and location, and depth on the performance of our predictive models. We also tested the method using field data from Black Hill norite, Australia, and Yeshan region, China, for which prior research results are available for comparison. Our study shows that machine learning provides an effective means of automatically predicting magnetization directions based on magnetic data maps.

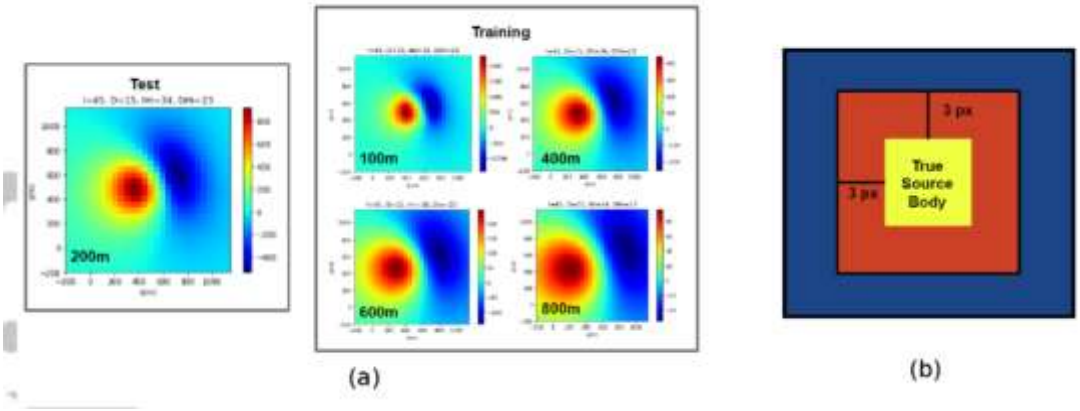

Figure 1. (a) Example data maps resulting from different depths (but with the same magnetization direction and magnitude). The test set is from the true model placed 200 m in depth, while the training set is from the source body placed in 4 different depths: 100m, 400m, 600m, 800m. (b) A schematic of the considered area to generate different lateral positions of the source body for the larger training set. In the synthetic case, 3 px represents an offset of 150 m beyond the true source body boundaries.

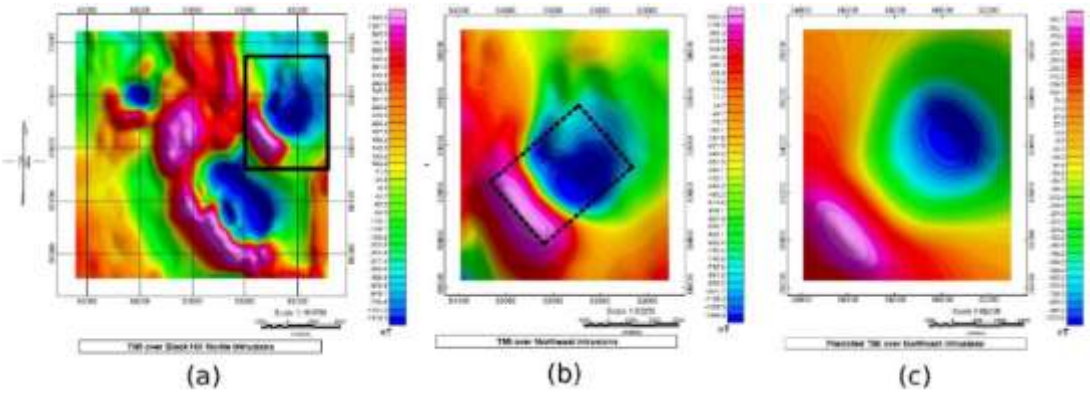

Figure 2. (a) The regional magnetic data map of the norite intrusion area. The boxed area indicates the area of our study. (b) The Black Hill Site data map with the inferred shape of the source body indicated by the dotted-lines. (c) A predicted data map calculated from the inferred source body shape using the predicted magnetization directions (magnetization inclination of 25° and magnetization declination of -135°)

7. 新仙女木事件的时间和结构及其潜在的气候动力

翻译人：杨会会 11849590@mail.sustech.edu.cn

Cheng H, Zhang H W, Spotl C et al. ***Timing and structure of the Younger Dryas event and its underlying climate dynamics****[J]. Proceedings of the National Academy of Sciences of the United States of America, 2020.*

https://doi.org/10.1073/pnas.2007869117

摘要：新仙女木事件（YD）可以说是被研究最广泛的千年尺度极端气候事件，其特征是全球不同的水文气候变化和高纬度地区的严重降温，它突然中断了末次冰期向现在间冰期的变暖趋势。到目前为止，对它的触发、传播和终止的精确理解仍然是难以捉摸的。本文提供了石笋氧同位素数据，再结合其他指标使我们能够以前所未有的次百年时间精度，量化 YD 事件横跨北大西洋、亚洲季风-西风带和南美季风区的发生和终止时间。我们的分析表明，北大西洋和亚洲季风西风带的 YD 事件基本上是同步的在几十年内发生（12870 ±30 B.P.），并触发了南极洲的 YD 事件。这一个由北向南的气候信号传递过程，通过大气（十年尺度）和海洋过程（百年尺度）传播，与 DO 事件在末次冰期的传递相似。相比之下，YD 事件的终止可能首先开始于南极约 11900 B.P.，或者可能更早开始于西热带太平洋，北大西洋紧随其后介于 11,700 ±40 和 11,610 ±40 B.P.之间。这些观测结果表明，最初的 YD 事件终止可能起源于南半球和/或热带太平洋，表明南半球/热带到北大西洋-亚洲季风-西风气候恢复的方向性。

ABSTRACT: The Younger Dryas (YD), arguably the most widely studied millennial scale extreme climate event, was characterized by diverse hydroclimate shifts globally and severe cooling at high northern latitudes that abruptly punctuated the warming trend from the last glacial to the present interglacial. To date, a precise understanding of its trigger, propagation, and termination remains elusive. Here, we present speleothem oxygen-isotope data that, in concert with other proxy records, allow us to quantify the timing of the YD onset and termination at an unprecedented subcentennial temporal precision across the North Atlantic, Asian

Monsoon-Westerlies, and South American Monsoon regions. Our analysis suggests that the onsets of YD in the North Atlantic (12,870 ± 30 B.P.) and the Asian Monsoon-Westerlies region are essentially synchronous within a few decades and lead the onset in Antarctica, implying a north-to-south climate signal propagation via both atmospheric (decadal-time scale) and oceanic (centennial-time scale) processes, similar to the Dansgaard – Oeschger events during the last glacial period. In contrast, the YD termination may have started first in Antarctica at ~11,900 B.P., or perhaps even earlier in the western tropical Pacific, followed by the North Atlantic between ~11,700 ± 40 and 11,610 ± 40 B.P. These observations suggest that the initial YD termination might have originated in the Southern Hemisphere and/or the tropical Pacific, indicating a Southern Hemisphere/tropics to North Atlantic–Asian Monsoon-Westerlies directionality of climatic recovery.

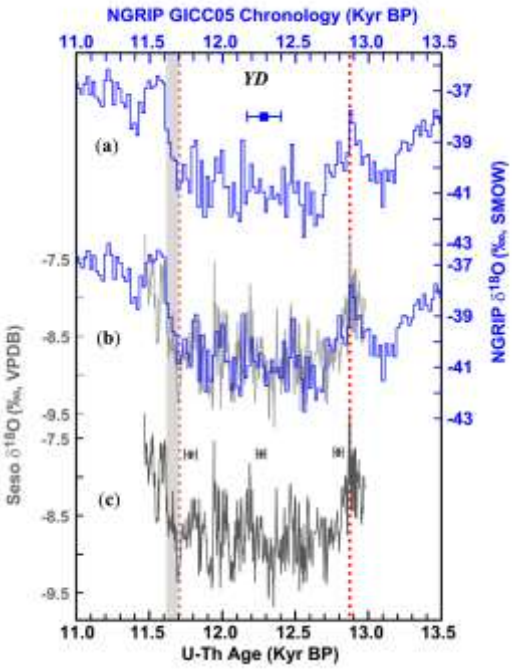

Figure 1. Comparison between Greenland NGRIP ice-core and Seso speleothem $\delta^{18}O$ records. (A, C) Greenland NGRIP (25) and Seso speleothem $\delta^{18}O$ records (this study), respectively. (B) Comparison between NGRIP (blue) and Seso (gray) $\delta^{18}O$ records. The error bars show the typical age error of each YD record (color-coded). The two vertical red dashed lines depict the initial onset (the abrupt drop at ~12,870 ± 30 B.P.) and initial termination (initiated at ~11,700 ± 40 B.P.) of the YD based on correlation of distinct features at subcentennial precision. The gray bar shows the YD termination excursion from ~11,700 to ~11,610 B.P. Kyr BP, 1 ×103 B.P.

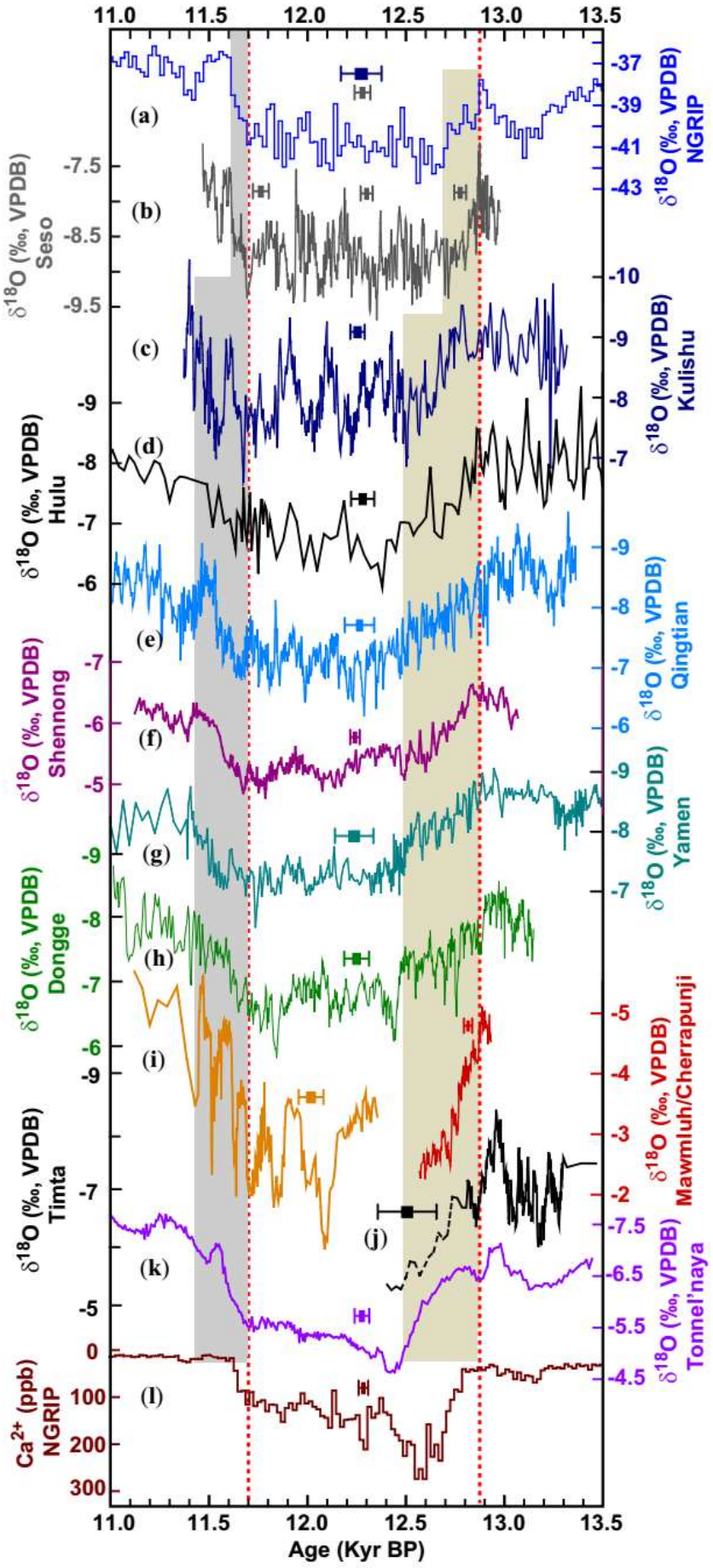
11.0
11.5
12.0
12.5
13.0
13.5
(a)
(b)
(c)
(d)
(e)
(f)
(g)
(h)
(i)
(j)
(k)
(l)
δ18O (‰, VPDB) NGRIP
δ18O (‰, VPDB) Seso
δ18O (‰, VPDB) Kulishu
δ18O (‰, VPDB) Hulu
δ18O (‰, VPDB) Qingtian
δ18O (‰, VPDB) Shennong
δ18O (‰, VPDB) Yamen
δ18O (‰, VPDB) Dongge
δ18O (‰, VPDB) Mawmluh/Cherrapunji
δ18O (‰, VPDB) Timta
δ18O (‰, VPDB) Tonnel'naya
Ca2+ (ppb) NGRIP
Age (Kyr BP)

Figure 2. Comparison of δ18O records from the North Atlantic, East AM, Indian Monsoon, and AW domains. (A, B) NGRIP δ18O on GICC05 chronology (25) and Seso $\delta^{18}O$ record from the North Atlantic, respectively. (C–H) Kulishu, Hulu (38), Qingtian (39), Shennong, Yamen (40), and Dongge $\delta^{18}O$ records from the East AM domain, respectively. (I) Mawmluh (yellow) and Cherrapunji (marron) $\delta^{18}O$ records from the Indian Monsoon domain. (J) Timta $\delta^{18}O$ record from the Indian Monsoon domain (41). (K) Tonnel'naya $\delta^{18}O$ record from the AW domain. (L) NGRIP Ca^{2+} on the GICC05 chronology (1) (SI Appendix, Fig. S1). Speleothem records are from this study except for those indicated by references. Error bars depict the typical age error of each record. Two vertical red dashed lines depict the initial onset (12,870 ± 30 B.P.) and termination (11,700 ± 40 B.P.) of the YD based on Seso and NGRIP $\delta^{18}O$ records. The vertical bars show durations of full-onset (beige) and termination (gray) excursions of the YD. Kyr BP, 1 × 103 B.P.

8. 中更新世以来亚洲季风的季节性干湿变化

翻译人：王浩森 11930841@mail.sustech.edu.cn

Wang X, Dettman D L, Wang M, et al. 2020. ***Seasonal wet-dry variability of the Asian monsoon since the middle Pleistocene. Quaternary Science Reviews [J], 247: 106568.***

https://doi.org/10.1016/j.quascirev.2020.106568

摘要：夏季湿润和冬季干燥是季风气候的基本特征，但是干湿季节性变化随着时间的改变的量化过程是很有挑战性的，因为大多数地质材料都无法记录一年一次的环境信号，而是以数年，数十年或几个世纪来代替。本文中我们利用高分辨率的中国黄土高原蜗牛壳的稳定氧同位素分析，对中更新世以来亚洲季风气候的干湿季节进行了量化。这种方法使我们可以收集地质历史中单个季节和年份的数据。现代贝壳记录表明：1）北方冬季（干旱）季节的 $\delta^{18}O_{shell}$ 值较高，而北方（夏季）潮湿的季节的 $\delta^{18}O_{shell}$ 值较低； 2）$\delta^{18}O_{shell}$ 的冬季和夏季差异（高达 19.2‰）远大于季节性温度变化所预期的差异； 3）壳内的 $\delta^{18}O$ 范围（最正值与最负值之间的差）记录了干燥季节蜗牛体内水分的蒸发程度，并结合了潮湿季节的降雨 $\delta^{18}O$/温度指示器。虽然我们需要更多工作来校准该指数，但该范围扔可作为干湿季节替代指数。黄土层中的 $\delta^{18}O_{shell}$ 范围（平均为 13.6‰）大于间冰期古土壤层的 $\delta^{18}O_{shell}$ 范围（平均 8.6‰），这表明自从中更新世以来的时期，冬季干旱存在显着差异。冰期冬季较干，间冰期较湿润。在冰期干燥的季节，西风侵入该地区可能改变了这种模式。在所有的记录中，夏季的最低 $\delta^{18}O_{shell}$ 值是相似的。但是，如果来自西风的一些水分在间冰期贡献了更多的负 $\delta^{18}O$ 值，那么这些最小的 $\delta^{18}O$ 值可能不会与石笋记录中看到的模式相矛盾。所以未来的工作应集中在蜗牛壳中同位素中。

ABSTRACT: Wet summers and dry winters are an essential feature of monsoon climates, but quantification of change in wet-dry seasonality through time is very challenging because most geological materials fail to record sub-annual environmental signals, instead integrating years, decades, or centuries. Here we quantify Asian wet-dry seasonality since the middle Pleistocene for

monsoon climates using high resolution stable oxygen isotope analysis of land snail shells from the Chinese Loess Plateau. This approach allows us to collect data on single seasons and years in geologic history. Modern shells show that: 1) the $d^{18}O$shell values are higher in boreal winter (dry) seasons and lower in boreal summer (wet) seasons; 2) winter e summer differences in d18Oshell (up to 19.2‰) are much larger than that expected from seasonal temperature variation; and 3) the d18Oshell range (the difference between the most positive and the most negative values) within a shell records the degree of evaporation of snail body water in the dry season, combined with a rainfall $d^{18}O$/temperature indicator in the wet season. This range can be used as a wetdry seasonality proxy index, although clearly more work is required to calibrate this index. d18Oshell ranges in glacial loess strata (mean ¼ 13.6‰) are systematically larger than those from interglacial paleosol layers (mean ¼ 8.6‰), suggesting that a significant difference in winter aridity was present, with drier winters in glacial periods and wetter winters in interglacial periods since the middle Pleistocene. This pattern may have been modified by the intrusion of the westerlies into the region in glacial dry seasons. Summer minimum d18Oshell values are similar throughout the record, which contrasts significantly with glacial/interglacial speleothem records, especially if these represent typical monsoon stable isotope patterns in rains. However, if some moisture from the westerlies contribute more negative $d^{18}O$ values in glacial intervals, these minimum $d^{18}O$ values may not contradict the patterns seen in the speleothem record. Future work should focus on the seasonal timing of the isotope cycles in land snail shells.

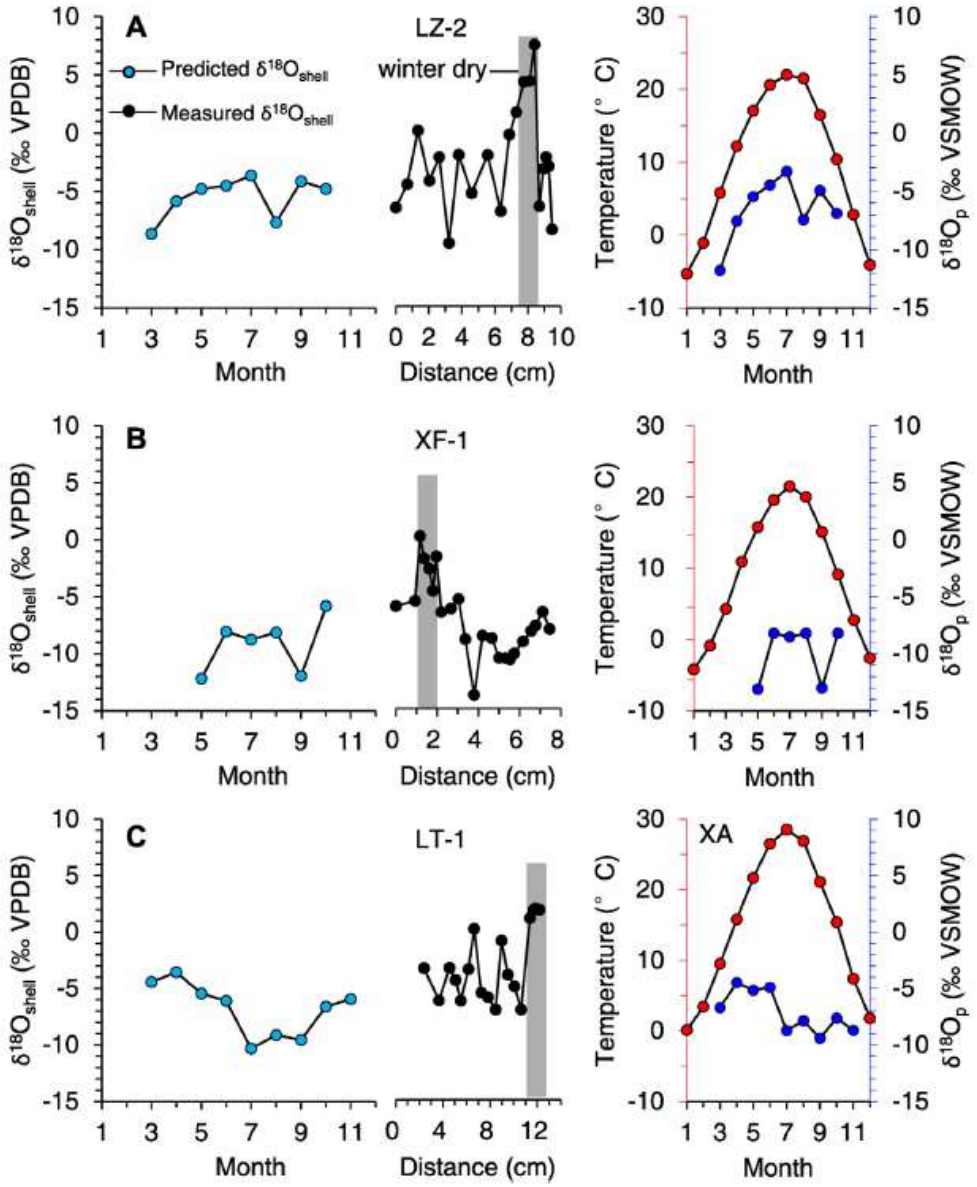

Figure 1. Comparison of measured $\delta^{18}O$ values of shells with predicted values. Predicted (left panels) and measured (middle panels) $\delta^{18}O$ values for land snail aragonite based monthly average temperature and $\delta^{18}O$ value of precipitation data from the IAEA database of isotopes in precipitation (shown at right) and the equilibrium fractionation factor for aragonitewater (Dettman et al., 1999). Dark gray bands are suggested cool climate intervals. Note that the minimum $\delta^{18}O$ values in the shells are similar to the minimum $\delta^{18}O$ values predicted within the seasonal cycle for the LZ and XF sites.

9. 末次冰期气候突变的一致时间

翻译人：郑威　11930589@mail.sustech.edu.cn

Corrick E C, Drysdale R N, Hellstrom J C, et al. ***Synchronous timing of abrupt climate changes during the last glacial period****[J].* ***Science****, 2020, 369(6506): 963-969.*

DOI: 10.1126/science.aay5538

摘要：所有末次冰期期间的气候突变都已经在全球的古气候记录中被探测到，但是我们对于这些气候突变发生的绝对时间和区域同时性的理解还不够完整。我们整理的63个已发表的独立定年的洞穴沉积物记录显示格陵兰岛的突然变暖与亚洲季风区、南美季风区和欧洲-地中海区域同时的气候变化（发生在几十年内）有关。结合大气响应的跷跷板效应解释，这些记录提供了暖事件期间高纬到热带气候变化耦合同时性的证据。我们的结果提供了一个全球一致性的框架，为气候突变的模型模拟提供依据，并且约束了冰芯的年代框架。

ABSTRACT: Abrupt climate changes during the last glacial period have been detected in a global array of palaeoclimate records, but our understanding of their absolute timing and regional synchrony is incomplete. Our compilation of 63 published, independently dated speleothem records shows that abrupt warmings in Greenland were associated with synchronous climate changes across the Asian Monsoon, South American Monsoon, and European-Mediterranean regions that occurred within decades. Together with the demonstration of bipolar synchrony in atmospheric response, this provides independent evidence of synchronous high-latitude–to-tropical coupling of climate changes during these abrupt warmings. Our results provide a globally coherent framework with which to validate model simulations of abrupt climate change and to constrain ice-core chronologies.

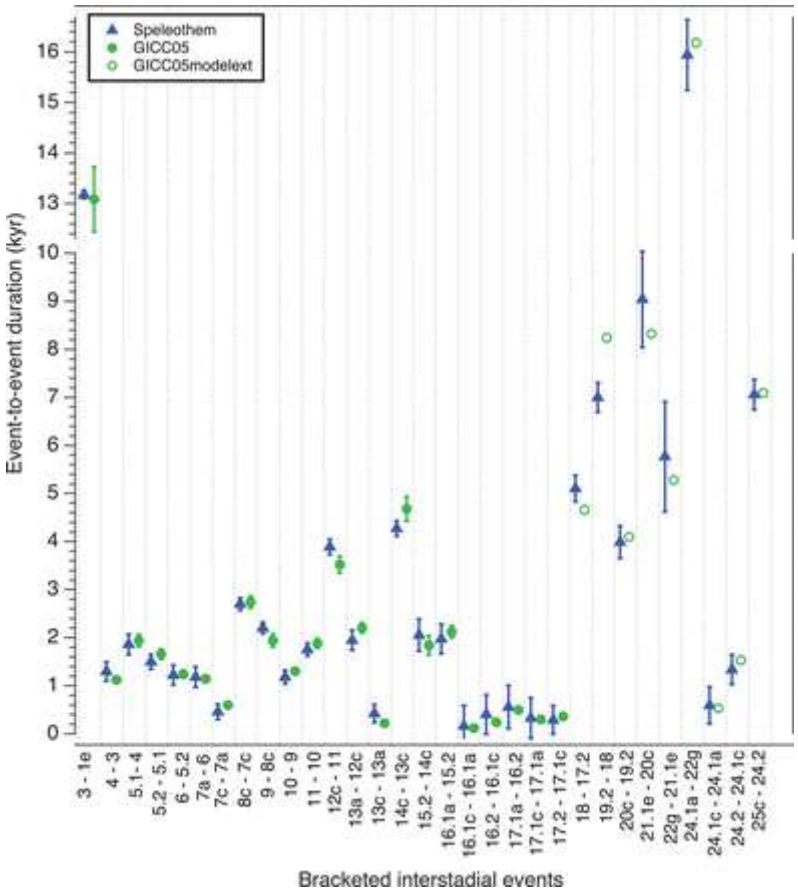

Figure 1. The time interval between the onset of consecutive interstadials in the GICC05/GICC05modelext chronology is compared with the corresponding interval based on the SIOC19 ages. Error bars represent the 2σ age uncertainties on the interval. For the GICC05 chronology, this was calculated as the change in the accumulated layer-counting uncertainty between events (fig. S1); errors are not shown for events within the GICC05modelext section because they are not quantified (*32*). For the speleothems, the error bar is the uncertainty of the consecutive SIOC19 age estimates in quadrature. The timing between interstadial onsets is shown for those interstadials demonstrated to be synchronous in the speleothems, including estimates based on data from only one region.

10. 基于地球系统模型模拟研究单次大型火山喷发引起的全球和极地温度变化

翻译人：张伟杰 12031188@mail.sustech.edu.cn

Liu B, Wang B, Liu J, Chen D, Ning L, et al. 2020. ***Global and Polar Region Temperature Change Induced by Single Mega Volcanic Eruption Based on Community Earth System Model Simulation****. Geophysical Research Letters.*

https://doi.org/10.1029/2020GL089416

摘要：为了了解单次大型火山喷发(SMVE)对全球和极地地区温度变化的长期影响。利用地球系统模型，选择公元 1258 年印度尼西 Samalas 特大火山喷发进行理想的模拟研究。重建和模拟都表明，Samalas 大型火山喷发之后北半球经历了近 20 年的强烈降温。北极显著的降温持续了 16 年，而南极只持续了两年。随着火山气溶胶逐渐消失，北极冬季出现更强的降温，而南极冬季出现变暖。SMVE 之后北极和南极这种不对称的温度变化是由与海冰相关的反射率反馈和海洋-大气热交换的综合效应造成的。

ABSTRACT: In order to understand the pure long‐term influence of single mega volcanic eruption (SMVE) of universal significance on global and polar region temperature changes, the AD 1258 Samalas mega volcanic eruption in Indonesia which is the largest eruption over the past millennium is selected as an ideal eruption for simulation study based on Community Earth System Model. Both reconstructions and simulations show that the Northern Hemisphere experienced nearly two decades of strong cooling after the Samalas mega eruption. The significant cooling in the Arctic lasts for 16 years, while the cooling in the Antarctic lasts only 2 years. As the volcanic aerosol gradually disappears, stronger cooling occurs in Arctic winter, and warming occurs in Antarctic winter. This asymmetric temperature changes over Arctic and Antarctic after SMVE (such as Samalas) are caused by the combined effects of albedo feedback and ocean -atmosphere heat exchange related to sea ice..

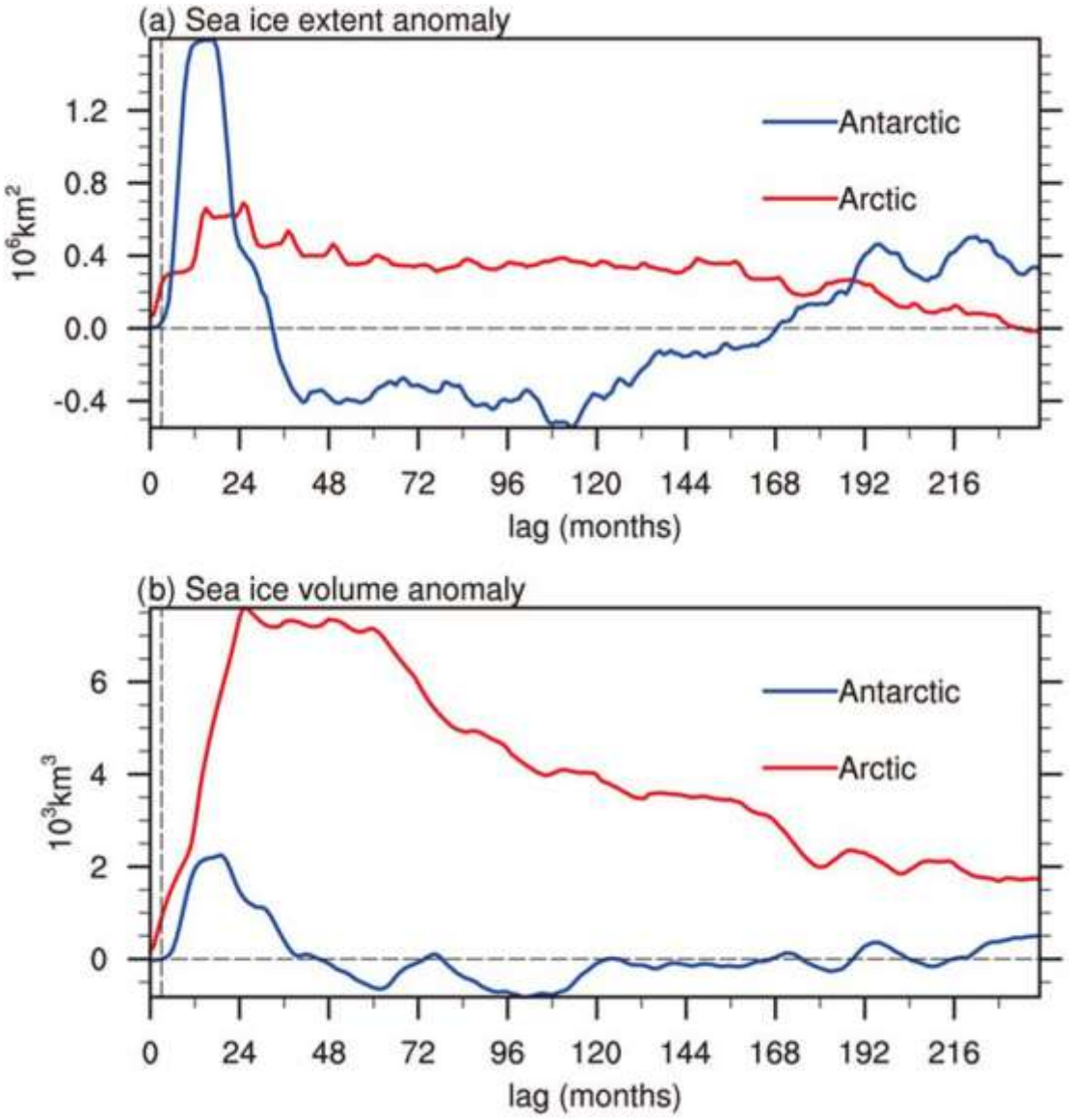

Figure 1. Simulated post-eruption anomalies of Arctic (60 ℃N-90 ℃N, red line) and Antarctic (60 ℃S-90 ℃S, blue line) sea ice extent (a) and sea ice volume (b). Anomalies are smoothed with a 13 - month moving average. The dashed vertical black lines indicate the start of the Samalas mega volcanic eruption in Vol. The lag (0) corresponds to January of the eruption year.

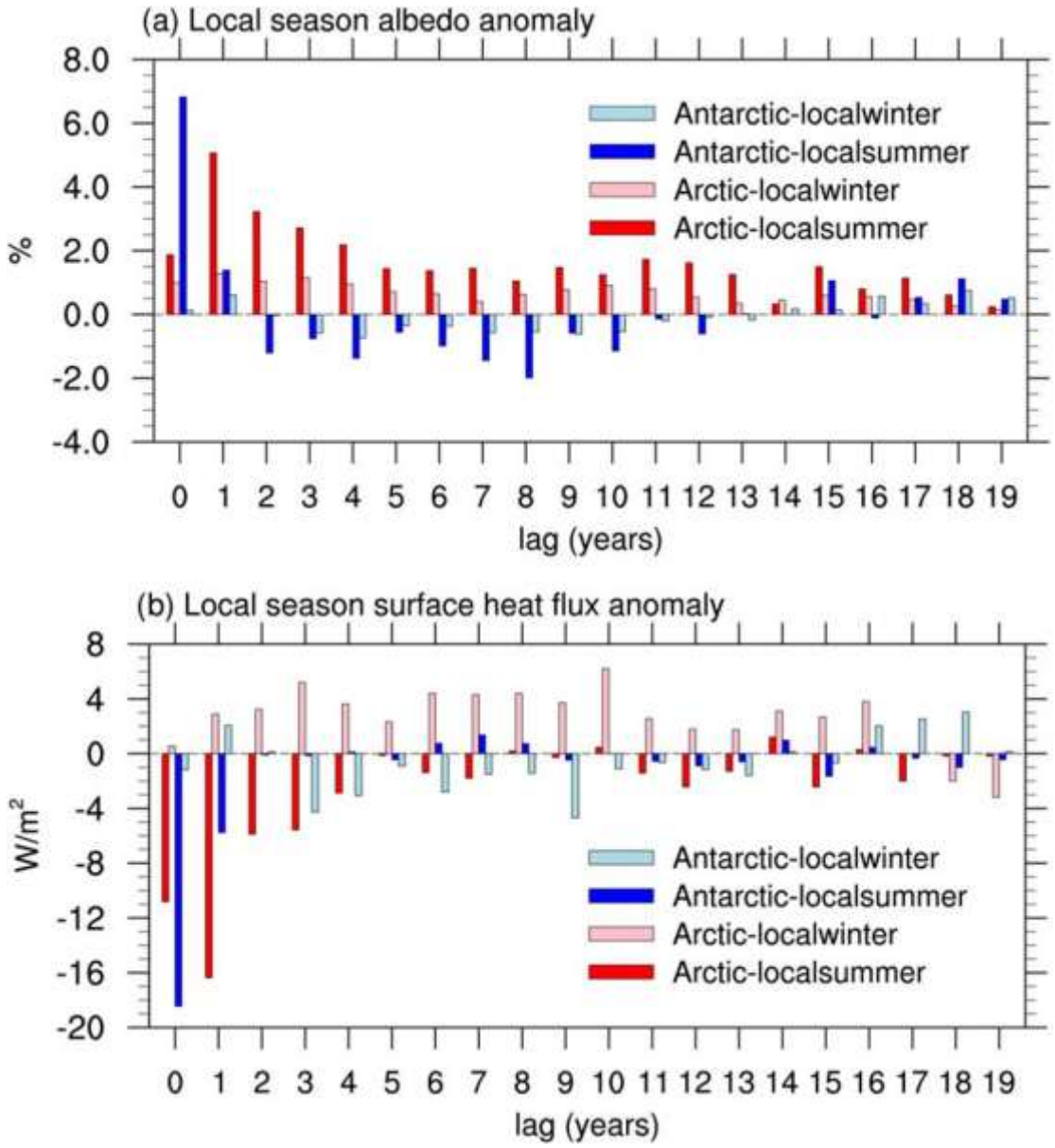

Figure 2. Simulated post‐eruption anomalies of Arctic (60°N–90°N) and Antarctic (60°S–90°S) local season albedo (a) and downward surface heat flux (b) over ocean area. Red bar and pink bar indicate Arctic local summer (May–September) and local winter (November–March), respectively. Blue bar and lightblue bar indicate Antarctic local summer (November–March) and local winter (May–September), respectively. The lag (0) corresponds to the eruption year. In (b), positive (negative) anomaly means ocean gains (loses) heat from (to) the atmosphere.

11. 第四纪晚期东亚非均质降雨变化对哈德利环流重组的响应

翻译人：李海 12031330@mail.sustech.edu.cn

Debo Zhao, Shiming Wan, Zhengyao Lu, Lina Zhai, Xuguang Feng, Xuefa Shi, Anchun Li. ***Response of heterogeneous rainfall variability in East Asia to Hadley circulation reorganization during the late Quaternary****[J]. Quaternary Science Reviews, 2020*

https://doi.org/10.1016/j.quascirev.2020.106562

摘要： 用中国洞穴沉积物 $\delta^{18}O$ 记录重建第四纪以来东亚地区夏季降水变化，结果显示东亚地区整体的一致性，长期以来被认为等同于季风强度。它的变化和全球气候的遥相关通常用 ITCZ 的子午位移来解释。但许多代用指标、气候模拟及气象观测表明东亚不同地区在多时间尺度上的降水模式不一致。东亚地区夏季降水的空间异质性表明该区的水文气候未因 ITCZ 的迁移而得到充分调整。我们报道了中国东海北部 400 ka 以来的降水变化的趁机记录，该记录与瞬态气候模型模拟相结合，表明东部中东南部地区降雨之间存在反相位关系亚洲和北亚和西南亚在进动带上，夏季的日照强度高，对应于北亚和西南亚东亚的降雨强度增加，而中东的降雨强度则降低。我们将东亚降雨的这种区域异质性归因于哈德利环流的重组，包括响应于半球子午温度梯度变化的上升分支（ITCZ）和下降分支（亚热带西风急流）的变化。我们的结果强调了哈德利环流在东亚水文气候中的关键作用，并对未来的气候预测具有重要意义。

Abstract: The Quaternary East Asian summer rainfall evolution reconstructed with the Chinese speleothem $\delta^{18}O$ records shows the consistency throughout the region of East Asia, and has long been considered equivalent to the monsoon intensity. Its variation and teleconnection with global climate were usually interpreted by the meridional shift of the intertropical convergence zone (ITCZ). However, many other proxy records, climate simulations and meteorological observations suggest the inconsistent rainfall patterns in the different regions of East Asia on multi-timescales. Such spatial heterogeneity in Quaternary East Asian summer rainfall indicates that the hydroclimate in this region is not fully paced by the migration of the ITCZ. Here, we report a sediment record of rainfall evolution during the last 400 ka in the northern East China Sea, and this record, in combination with a transient climate model simulation, indicates an out-of-phase relationship between rainfall over middle-southeastern East Asia and northern and southwestern East Asia on the precession band, with high boreal summer insolation corresponding to the

increased rainfall intensity in the northern and southwestern East Asia, however, decreased rainfall intensity in the middle East Asia. We attribute this regional heterogeneity in East Asian rainfall to the reorganization of the Hadley circulation, including shifts in the ascending branch (ITCZ) and descending branch (subtropical westerly jet), in response to changes in the hemispheric meridional temperature gradient. Our results highlight the crucial role of the Hadley circulation in the East Asian hydroclimate and have important implications for future climate projections.

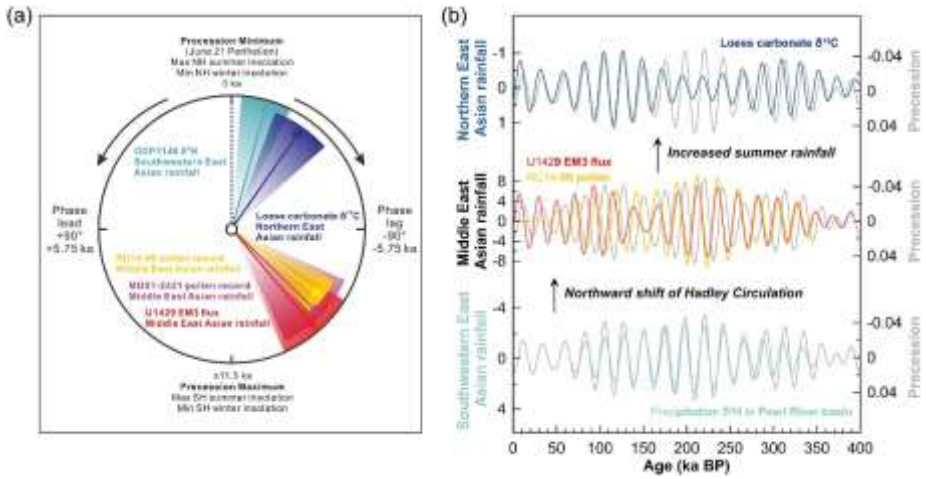

Figure 1. Phases of rainfall evolution in different regions of East Asia. (a) Phase wheel of rainfall proxies on the precession band. The precession index is defined as $\Delta\varepsilon\sin\omega$, where ω is the longitude of the perihelion measured from the moving vernal point and ε is the eccentricity of Earth's orbit around the Sun. The loess carbonate δ13C has been multiplied by −1 prior to phase calculation. Phases of all rainfall proxies are coherent at 95% confidence interval, and phase error shown with shading. The "+" and "-" indicate phase lead and lag, respectively. (b) Comparison of precession and 23-ka bandpass-filtered rainfall proxies in the East Asia.

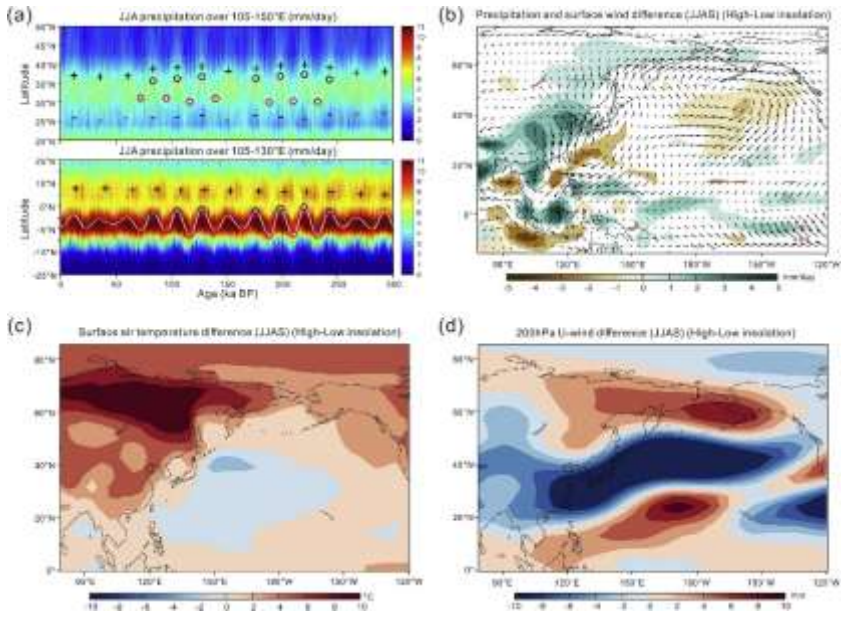

Figure 2. Simulated spatial and temporal change of rainfall, surface temperature and northern westerlies. (a) June–August rainfall distribution in the subtropical (20–50 °N, 105–150 °E) and tropical (25 °S–25 °N, 105–130 °E) region during the last 300 ka. White curves indicate the precession. (b) June–September rainfall and surface wind difference between high and low insolation during the last 300 ka. (c, d) The same as b, but for the surface air temperature and 200 hPa U-wind differences, respectively. In b-d, the high and low insolation composites of mean climate are calculated based on seven periods of relatively stronger precession modulation, which are marked in red and blue circles.

12. 始新世暖期气候敏感性的状态依赖证据

翻译人：张亚南 yananzhang@scsio.ac.cn

E. Anagnostou, E. H. John, T. L. Babila et al., ***Proxy evidence for state-dependence of climate sensitivity in the Eocene greenhouse*** *[J]. Nature Communication, 2020, 11, 4436. https://doi.org/10.1038/s41467-020-17887-6x.*

摘要：尽管现在研究进展的不断推进，大气 CO2 演化和气候之间的关系依然尚不确定。模拟研究表明，始新世早期显著的全球变暖特征，需要温暖气候状态对 CO2 强迫相比寒冷气候状态更为敏感。我们通过结合一种新的高分辨率 B 同位素 CO2 记录和全球平均气温的最新评估，来检测这一主张。我们发现平衡气候敏感度（Equilibrium Climate Sensitivity, ECS）在始新世极热时期的确更高，并且随着始新世变冷而下降，这很好的支持了最新的模拟研究结果。这些结果表明 IPCC 对 ECS 的标准范围（1.5-4.5℃ per doubling）不太可能符合过去高 CO_2 水平的温暖时期，ECS 的状态依赖性可能随着未来全球气候的变暖发挥着越来越重要的作用。

ABSTRACT: Despite recent advances, the link between the evolution of atmospheric CO2 and climate during the Eocene greenhouse remains uncertain. In particular, modelling studies suggest that in order to achieve the global warmth that characterised the early Eocene, warmer climates must be more sensitive to CO2 forcing than colder climates. Here, we test this assertion in the geological record by combining a new high-resolution boron isotope-based CO2 record with novel estimates of Global Mean Temperature. We find that Equilibrium Climate Sensitivity (ECS) was indeed higher during the warmest intervals of the Eocene, agreeing well with recent model simulations, and declined through the Eocene as global climate cooled. These observations indicate that the canonical IPCC range of ECS (1.5 to 4.5 ℃ per doubling) is unlikely to be appropriate for high-CO2 warm climates of the past, and the state dependency of ECS may play an increasingly important role in determining the state of future climate as the Earth continues to warm.

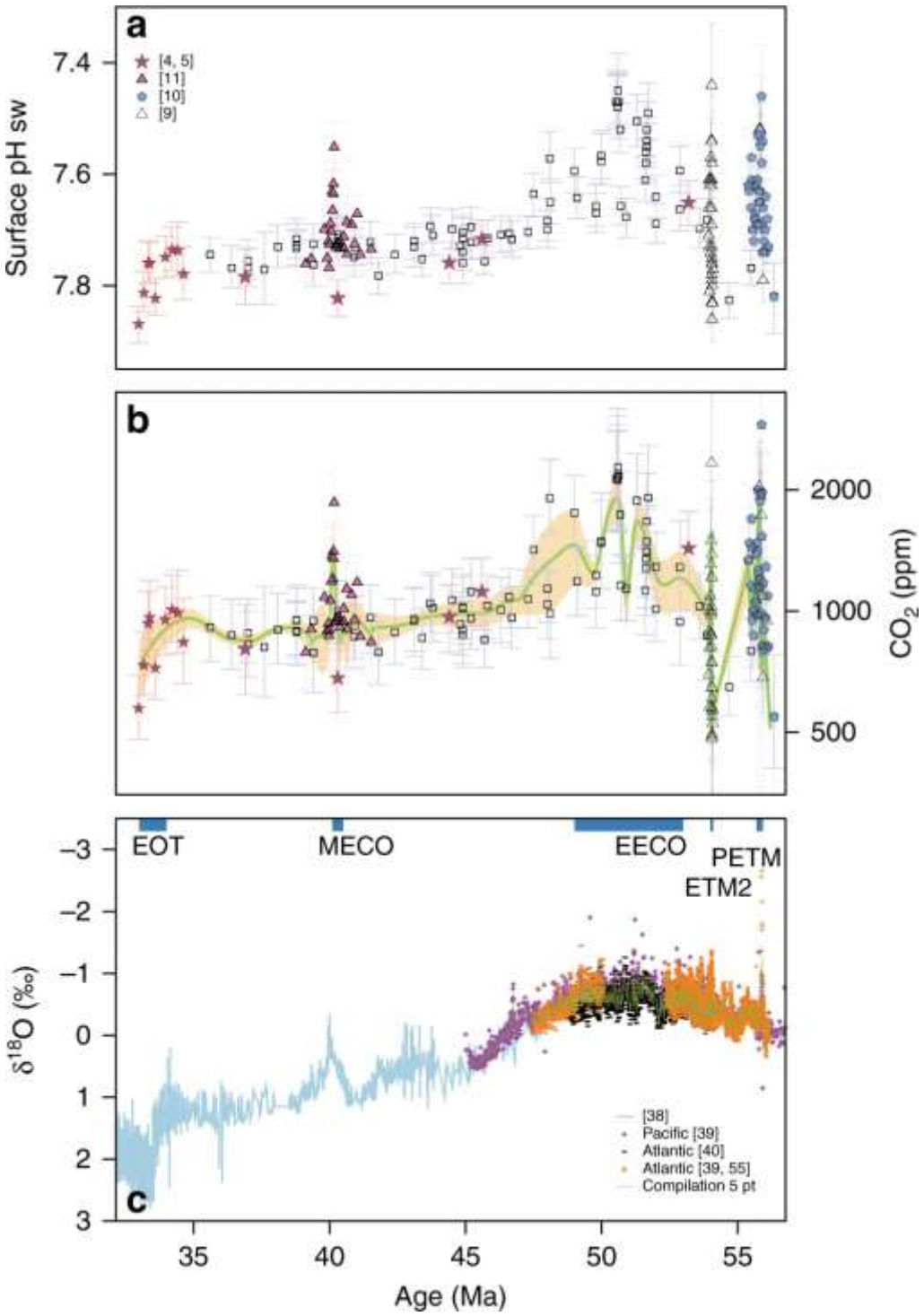

Figure 2. Compilation of $\delta^{11}B$ and $\delta^{18}O$ derived records for the Eocene. **a**, Seawater pH from the new $\delta^{11}B$ data presented here (black squares) and compiled from the literature. **b**, calculated atmospheric CO2 from the data shown in a, the LOESS fit (green line) and 95% confidence (orange shading). **c**, δ18O from benthic foraminifera are based on compilations. Error bars in **a**, **b** are 95% confidence. Intervals of time referred to in the text are shown as blue bars in **c**, labelled with appropriate acronym.

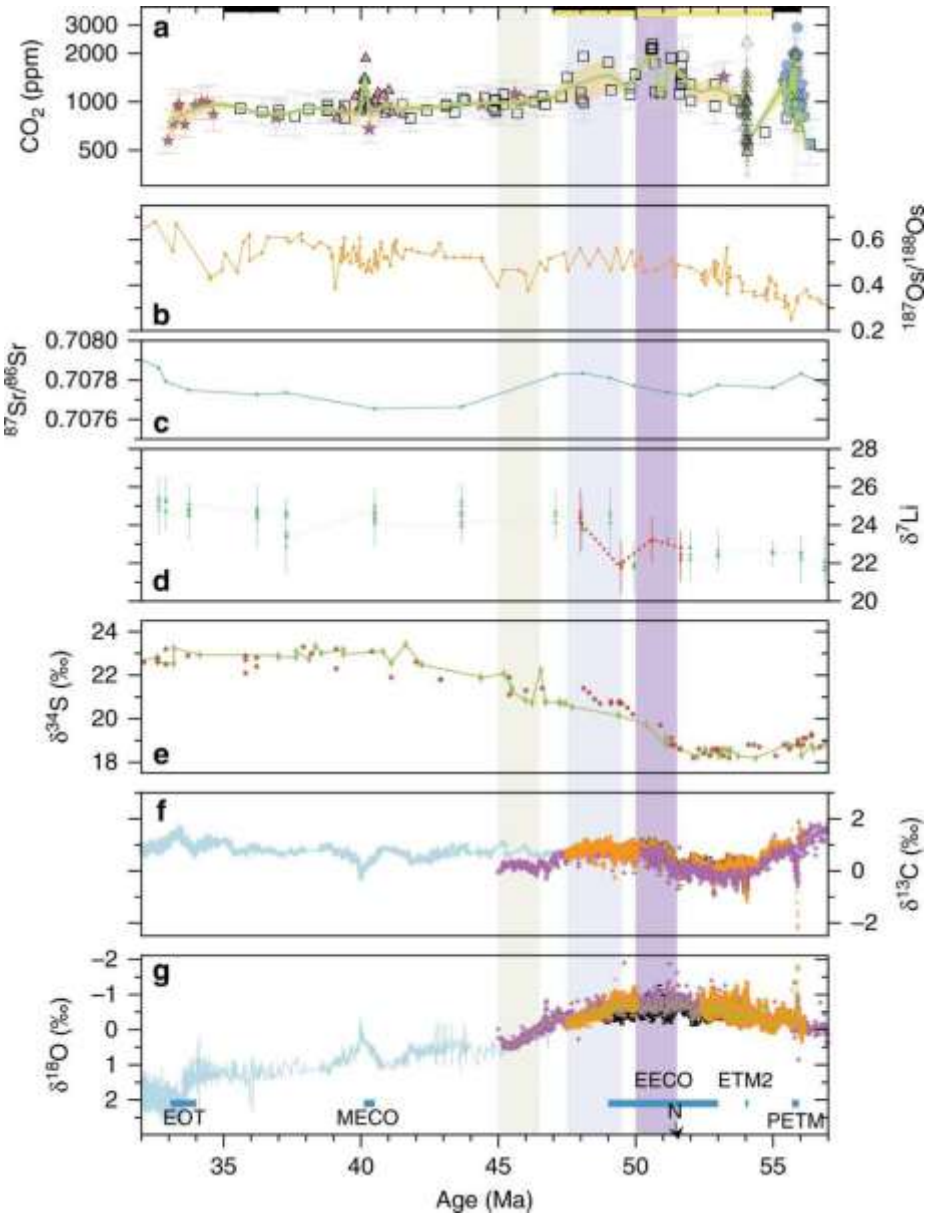

Figure 3. Early Eocene weathering, organic carbon burial and circulation changes. **a** The CO2 record as in Fig. 2. **b** The marine $^{187}Os/^{188}Os$ compilation. **c** the marine $^{87}Sr/^{86}Sr$ record. **d** The marine $\delta^{7}Li$, with red symbols/line updated to the same age model as for the CO_2 and $\delta^{18}O$ data. **e** The marine $\delta^{34}S$ (red circles), with the updated age model to GTS2012 (green circles). **f**, **g** Marine carbonate $\delta^{13}C$ and $\delta^{18}O$, color coding refers to the same references as in Fig. 2c. Purple bar envelopes the $\delta^{34}S$ increase, and "N" indicates the preceding CIE within C23n.2nH139. Light blue bar indicates the timing of temperature and CO_2 decline after the EECO. Green light bar indicates the timing of potential circulation changes in the early Eocene, as demonstrated in the $\delta^{13}C$ record of **f**. Overlying solid black and yellow bars represent the timing of volcanism.

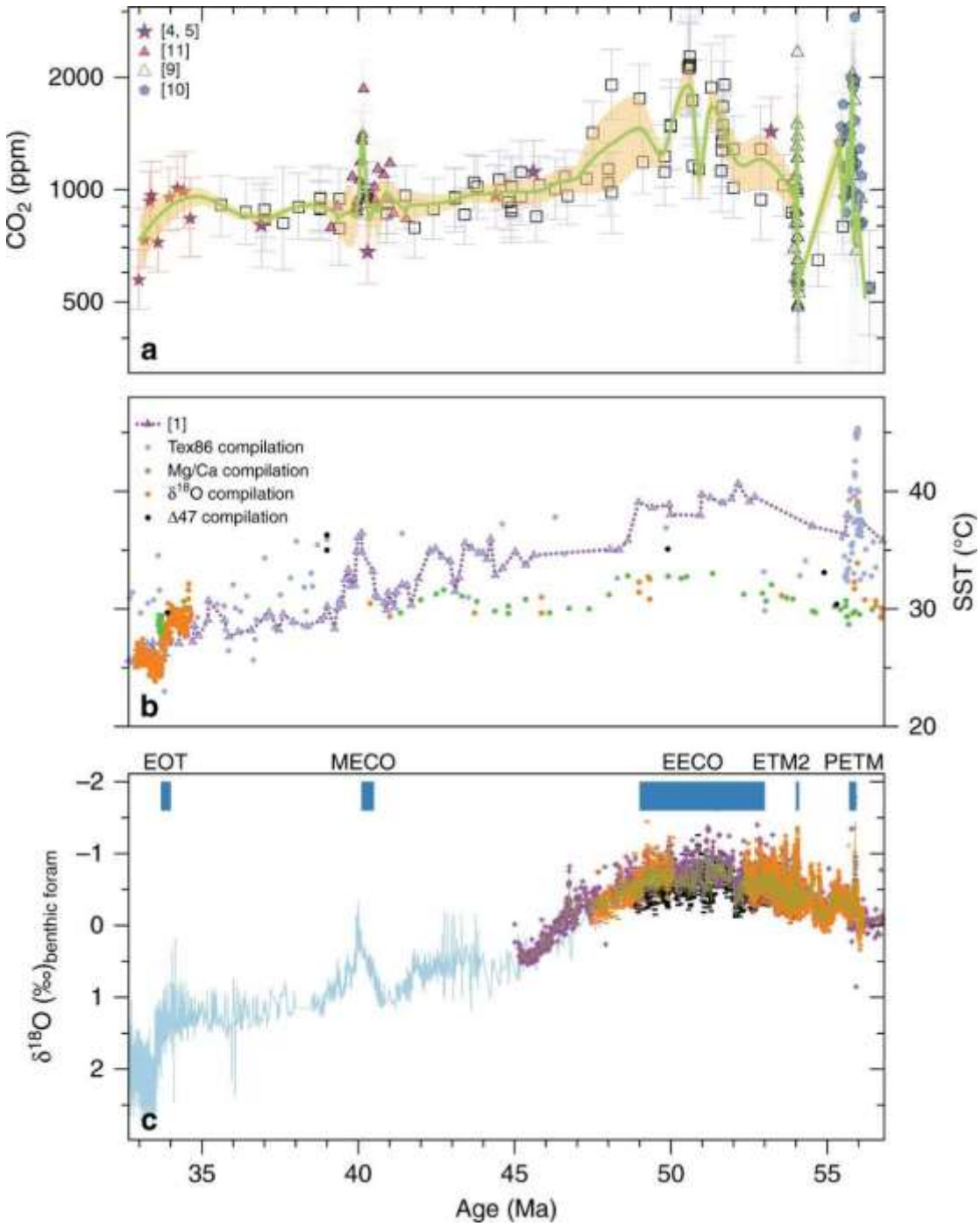

Figure 4. Comparison of the $\delta^{11}B$-derived CO_2 to temperature records. **a** CO_2 compilation as in Fig. 2**a**. **b** Sea surface temperature (SST) records. Purple dotted line connects the TEX_{86} record from ODP 9591. **c** Benthic foraminifera $\delta^{18}O$ (related to deep water temperature) as in Fig. 2**c**.

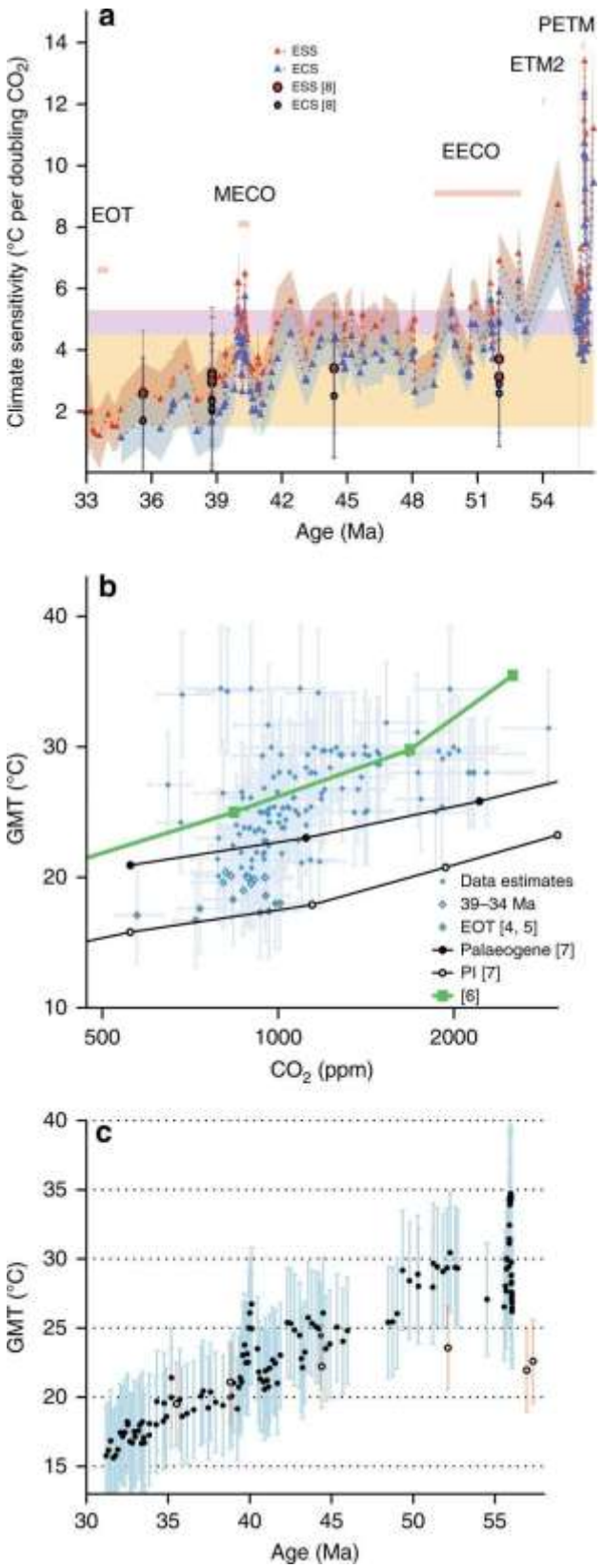

Figure 5. Evolving climate sensitivity for the Eocene. **a** Calculated ESS (red triangles and error envelope), and ECS (blue triangles and error envelope). See text for relevant methodology. Orange area

represents the IPCC range in ECS95, and the pink highlighted area the updated 20th century ECS with the addition of state-of-the-art cloud physics. Circles represent estimates. **b** Data-model inter-comparison, with all diamonds representing data. Open diamonds are the data between 39 and 34 Ma, and orange filled diamonds the EOT. Circles and squares are all model derived relationships (PI preindustrial). Uncertainties and error envelopes represent 1 s.d. of Monte Carlo propagated uncertainties. **c** Evolving GMT relationship for the Eocene. GMT is calculated using the BAYSPAR TEX86 record from ODP 959. Error bars represent the calibration and analytical uncertainty on TEX86. For comparison, the GMT estimates are presented with open symbols and red error bars. NB the elevated ECS early in the PETM and ETM 2 are most likely a consequence of slight age model misalignments, or imply non-CO2 forcing early in these events.